



Generalized Sparse Variation Regularization for Large Fluorescence Image Deconvolution

Hoai-Nam Nguyen, Vincent Paveau, Cyril Cauchois, Charles Kervrann

► To cite this version:

Hoai-Nam Nguyen, Vincent Paveau, Cyril Cauchois, Charles Kervrann. Generalized Sparse Variation Regularization for Large Fluorescence Image Deconvolution. 2017. hal-01609810

HAL Id: hal-01609810

<https://inria.hal.science/hal-01609810>

Preprint submitted on 4 Oct 2017

HAL is a multi-disciplinary open access archive for the deposit and dissemination of scientific research documents, whether they are published or not. The documents may come from teaching and research institutions in France or abroad, or from public or private research centers.

L'archive ouverte pluridisciplinaire **HAL**, est destinée au dépôt et à la diffusion de documents scientifiques de niveau recherche, publiés ou non, émanant des établissements d'enseignement et de recherche français ou étrangers, des laboratoires publics ou privés.

Generalized Sparse Variation Regularization for Large Fluorescence Image Deconvolution¹

Hoai-Nam Nguyen¹, Vincent Paveau², Cyril Cauchois², Charles Kervrann¹

¹ Inria, Centre Rennes-Bretagne Atlantique, SERPICO Project Team, 35042 Rennes, France

² Innopsys Inc., Carbonne 31390, France

Abstract

In this work, we generalize the sparse variation (SV) combining the total-variation (TV) and the L_1 regularization and introduce a novel family of convex and non-quadratic regularizers for fast deconvolution of large 2D fluorescence images. These regularizers are defined as mixed L_ν - L_2 norms ($\nu \geq 1$) which group image intensity and spatial differentials, computed at each pixel of the image. By coupling a regularization term of this family with a quadratic data fidelity term, we propose a fast and efficient deconvolution method by using the primal-dual (proximal) algorithms to minimize the corresponding energy functional. Experiment results on both 2D simulated and real fluorescence scanner images demonstrate the performance of our method in terms of restoration quality as well as computational time.

Keywords : Fluorescence imaging, image deconvolution, sparse variation, convex optimization, proximal algorithms

1 Introduction

Fluorescence microscopy is nowadays an imaging technique widely used in the field of biomedical sciences for cell biology research. The sample of interest is first labelled by fluorescent molecules before being excited by the illumination light of a given wavelength ; upon the excitation, fluorophore re-emits light of relatively longer wavelength which is then collected by photosensitive sensors to form the digitized image of the input sample. This imaging modality provides in practice a very powerful framework to biologists for observing, analyzing, and studying specific fluorescently-tagged structures at very high spatial and temporal resolutions.

Despite number of advantages, there are two major limitations of fluorescence microscopy. The first limitation is the presence of noise in acquired images. Similarly to other optical imaging techniques, the main contribution of noise here is the photon (shot) noise. The latter is mainly due to the quantum nature of light, implying that the arrival of a photon on a sensor is a random event and thus the number of incident photons over a period of time is a random variable depending on the brightness of the light source. In the context of fluorescence imaging, the image signal-to-noise-ratio (SNR) is usually very low because the low dose of illumination light is required

1. This work was supported by Innopsys Inc.

to avoid photo-bleaching of fluorescent molecules and preserve specimen integrity (photo-toxicity). Additionally, the quality of acquired fluorescence images is worsened by the blurring effect. This second limitation (i.e. blur) is a consequence of various factors during acquisition process including optical diffraction, excitation wavelength, immersion medium refraction and specimen thickness. These limitations not only degrade the image quality in terms of overall visualization but also have a negative severe impact on specimen analysis since they reduce the ability to recognize the objects of interest from noisy background and to detect fine details.

To improve the quality of images acquired by fluorescence microscopes, deconvolution is frequently suggested as pre-processing step for noise removal and resolution enhancement before further analysis. It aims at restoring the original (noise-free and sharp) image from observed noisy and blurry image, which is in general an ill-posed inverse problem. Number of regularization-based methods have been proposed over the past few decades in order to stabilize numerically the solution of the underlying inverse problem as well as to produce better estimation in the sense that the latter looks more similar to real-world images. The choice of an appropriate regularization modelling prior knowledge about the imaged objects is thus highly important for high-quality deconvolution results.

In this paper, we present a novel family of convex regularizers which are well-suited for fluorescence microscopy images by taking into account the characteristics of fluorescence imaging context. These regularizers are inspired from the concept of sparse variation (SV), originally introduced by Eickenberg *et al.* for MRI segmentation [1]. Indeed, based on the observation of the sparse distribution and the co-localization of regions with high intensity and high-magnitude gradient on fluorescence images, we consider the mixed norm L_1 - L_2 norm of a linear transform combining the image intensity and spatial differential coefficients into one feature vector, computed at each pixel of the image, to promote the spatial sparsity of bright objects over relatively darker background. Under the assumption of additive Gaussian noise, the image deconvolution problem then corresponds to the minimization of a convex functional which can be efficiently solved by primal-dual (proximal) algorithms. We evaluate furthermore the proposed SV-based deconvolution method on both simulated and real fluorescence images. Experimental results prove that our regularization approach outperforms total variation (TV) [2] which is the most widely used regularizer in image processing, and is very competitive when compared to the Hessian Schatten-norm regularizer [3].

The remainder of the paper is organized as follows. In Section 2, we briefly review several existing deconvolution methods for bi-dimensional (2D) fluorescence microscopy images. In Section 3, we introduce the norm-based regularization approach which is frequently used in image processing. We derive a novel family of convex non-quadratic regularizers by generalizing the concept of sparse variation. In Section 4, given the family of regularizers, a general variational framework for image deconvolution is presented. We also describe an optimization algorithm to solve the underlying variational problem. Then, in Section 5, we assess the performance of our approach on simulated and real large fluorescence images. Finally, we conclude this paper and propose some future work in Section 6.

2 Related works for deconvolution of fluorescence images

In fluorescence microscopy, the arising blur is mainly induced by the limited aperture of the objective which results in light diffraction through the optical system. The diffraction phenomenon implies that light emitted by an infinitely small point source appears wider at the focal plan and spreads into a specific pattern called “point spread function” (PSF). As a consequence, the obtained 2D image of an object is the superposition of these emitted light patterns from each point of the

object. It can be mathematically modelled as the convolution product of the imaged object and the PSF of the microscope under the linear shift-invariance assumption of the imaging system. In contrast with hardware-assisted techniques that aim at adjusting the optical system to reduce the size of the PSF and/or reject out-of-focus light before it reaches the detector, hence improving the spatial resolution of acquired images, deconvolution is a computational post-processing technique which consists in restoring a sharper image of the object from its blurry digitized version.

In the last twenty years, many deconvolution methods have been investigated in order to deal with the steadily increasing amounts of microscopy data. The most popular deconvolution approach is the linear filtering method such as Wiener and Tikhonov-Miller [4, 5, 6] filters. The former provides the minimizer of the mean squared error between the estimated (deconvolved) image and the true image, while the latter consists in minimizing an energy functional composed of a quadratic data term and a quadratic regularization term, resulting in linear operations on the acquired image. Both Wiener and Tikhonov-Miller filters assume that the acquired image is corrupted by additive Gaussian noise. Despite the simplicity and low-computation-requirement, such linear methods usually produce limited deconvolution results since they do not restore fine image details at frequency components that are beyond the bandwidth of the point spread function (*i.e.* the support of its Fourier transform). Moreover, the positivity of the results obtained with these filters can not be always guaranteed due to their linear nature. It presents therefore a major issue while dealing with fluorescence microscopy images in which pixel intensities have positive values by definition.

To handle this issue, several iterative non-linear algorithms have been proposed instead of previously mentioned one-step approaches. Among them, the iterative constrained Tikhonov-Miller algorithm [4, 5, 6] and a modified version of it which is called the Carrington algorithm [7, 8] consist in minimizing iteratively the Tikhonov functional. The only difference between them is in the way they integrate the constraint of non-negativity at each iteration. In contrast with these additive-form algorithm, the Gold-Meinell algorithm [9] implicitly incorporates the positivity by considering a multiplicative formulation. As an alternative, the Richardson-Lucy algorithm [10, 11, 12] which is derived from the maximum likelihood estimation (MLE) under the assumption of Poisson noise involves similar multiplicative-form iterations. An important drawback of both Gold-Meinell and Richardson-Lucy algorithms is however their numerical instability, resulting in noise amplification after a small number of iterations. A further review of these classical deconvolution algorithms is given in [13].

Later on, the total variation (TV) regularization approach, originally introduced by Rudin, Osher and Fatemi for image denoising [2], was widely used for image deconvolution [14], including in microscopy imaging [15, 16]. The success of this well-known approach is mainly due to its ability to preserve sharp edges and smooth homogeneous areas in the underlying images. Although, its downside is the staircasing effect, resulting in images of contiguous regions with constant intensities [17]. This effect is rather an artifact than a desired property on non-synthetic images. A family of non-quadratic functionals which involve Schatten norms of the Hessian matrix has been investigated in [3] as second-order extensions of TV in order to attenuate staircasing effect. Its performance was furthermore depicted in [18, 19] showing their effectiveness in biomedical applications, specially for fluorescence image deconvolution. Beside these Hessian-based regularizers, other second and higher-order regularization approaches were also proposed as alternatives, including the L_1 norm of the Laplacian operator, the modified Laplacian and the affine total-variation (see [3] for comprehensible comparison). Recently, a novel energy functional has been introduced using a specific non-convex regularization functional [20] to cope with the relevant characteristics of fluorescence images. This functional tends to penalize jointly the pixel intensities and intensity variations to favor sparsely distributed bright objects over relatively darker background. However, its non-convex nature leads

to complicated optimization problems and does not guarantee the convergence to global optimum. A gentle initialization of the algorithm is suggested in [20] to overcome local minima of the energy functional. An appropriate regularizer which takes into account important characteristics of fluorescence imaging in a similar way as in [20], and possesses interesting mathematical properties, including convexity, invariance to contrast, scale, rotation, and translation as total variation and Hessian Schatten norm regularizers, is therefore highly recommended for fast and high-quality deconvolution of large fluorescence images.

3 Norm-based regularization

Most of commonly-used regularizers in imaging problems (such as denoising, deconvolution, inpainting, etc.) have the following form :

$$E_R(u) = \int_{\Omega} \Phi(Lu(\mathbf{x})) \, d\mathbf{x} , \quad (1)$$

where u is an image defined on a square domain $\Omega \subset \mathbb{R}^2$, L (called “regularization operator”) is a linear operator used to control the spatial distribution of u and $\Phi(\cdot)$ is a positive potential function usually related to a norm distance. A typical example is the Tikhonov regularization using the squared Euclidean (L_2 -) norm chosen as potential function ($\Phi = \|\cdot\|_2^2$), frequently combined with the identity operator ($L = \text{Id}$) or a differentiation operator (such as the gradient and the Laplacian operators) or eventually a orthogonal projection operator in order to cope with particular structure of the desired solution. Due to their convex and differentiable properties, quadratic penalties are widely used for many years to numerically stabilize inverse problems arising in number of applications including astronomy [21, 22], ultrasound imaging [23], scanning-tunneling microscopy [24], electrical tomography [25], magnetic resonance imaging [26] and atomic-force microscopy [27]. Nevertheless, despite its mathematical tractability and implementation simplicity, Tikhonov regularization yields unsatisfactory results if the image transform (by the regularization operator L) does not have a small norm. In particular, when differentiation operator is used, it tends to produce blurred details in obtained images since images with low gradient magnitudes are encouraged.

3.1 Differential norm regularizers

To avoid over-smoothing caused by quadratic functionals, non-quadratic regularizers have been studied recently as alternative solutions. One of the most popular among them is total variation [2] which considers the gradient operator and the Euclidean norm as the following :

$$\text{TV}(u) = \int_{\Omega} \|\nabla u(\mathbf{x})\|_2 \, d\mathbf{x} , \quad (2)$$

where $\nabla u(\mathbf{x}) \in \mathbb{R}^2$ denotes the gradient of u at the point \mathbf{x} . By definition, total variation can be interpreted as the L_1 -norm of the image gradient magnitude $\|\nabla u\|_2$; or in other words, it corresponds to the mixed L_1 - L_2 norm ($\|\cdot\|_{1,2}$) of the image gradient ∇u where the L_1 -norm acts on the spatial domain Ω and the L_2 -norm acts on the gradient vector components. The use of the L_1 -norm, which promotes sparsity, favors images with vanishing gradients except at some points and thus allows to restore well-preserved and sharp edges, showing the superior performance of TV when compared to the Tikhonov approach. The convexity of such a norm enables to consider efficient optimization algorithms [28] and explains the wide use of total variation in various imaging applications due to

its computational simplicity. However, the drawback of TV is the staircasing effect (also known as blocking artifact) since imposing vanishing gradients also leads to piecewise-constant reconstructions while the underlying images are not necessary piecewise-constant.

A way to prevent the blocking artifact is to “regularize” the TV functional by replacing the Euclidean norm of the image gradient by a smooth approximation [29] of the following form :

$$\text{TV}_{h_\epsilon}(u) = \int_{\Omega} h_\epsilon(\|\nabla u(\mathbf{x})\|_2) \, d\mathbf{x} \, , \quad (3)$$

where $h_\epsilon : \mathbb{R}_+ \rightarrow \mathbb{R}$ is a smooth and non-decreasing function on \mathbb{R}_+ and ϵ is a parameter controlling the smoothness of the approximation. An usual and convenient choice for h_ϵ is the Huber function

$$t \mapsto \begin{cases} \frac{1}{2\epsilon} t^2 & \text{if } |t| \leq \epsilon \, , \\ |t| - \epsilon & \text{if } |t| > \epsilon \, , \end{cases} \quad (4)$$

which leads to the so-called “Huber norm”. This “norm” has similar behavior as the Euclidean norm for high gradient (when $\|\nabla u\|_2 > \epsilon$) but is quadratic for small gradient and thus implies the property of avoiding the blocking artifact of the associated TV-Huber (TVH) regularizer. The performance of TV-Huber model has been proved in [30] for image denoising.

Another way to overcome the issue of staircasing is to consider higher-order differentiation operators instead of first-order operators. By investigating the Hessian operator which is a second-order operator, Lefkimmiatis *et al.* proposed a family of convex regularizers as an extension of total variation [3]. It is based on the matrix norm of the Hessian, computed at each point of the image

$$\text{HV}_p(u) = \int_{\Omega} \|\mathcal{H}u(\mathbf{x})\|_{\mathcal{S}_p} \, d\mathbf{x} \, , p \geq 1 \, , \quad (5)$$

where $\mathcal{H}u(\mathbf{x})$ is the Hessian matrix of u at the point \mathbf{x}

$$\mathcal{H}u(\mathbf{x}) = \begin{bmatrix} \frac{\partial^2}{\partial x^2} u(\mathbf{x}) & \frac{\partial^2}{\partial x \partial y} u(\mathbf{x}) \\ \frac{\partial^2}{\partial y \partial x} u(\mathbf{x}) & \frac{\partial^2}{\partial y^2} u(\mathbf{x}) \end{bmatrix} \, , \quad (6)$$

and $\|\mathcal{H}u(\mathbf{x})\|_{\mathcal{S}_p}$ denotes its Schatten p -norm [31] defined as

$$\|\mathcal{H}u(\mathbf{x})\|_{\mathcal{S}_p} = \left(\sum_{l=1}^2 \sigma_l^p(\mathcal{H}u(\mathbf{x})) \right)^{\frac{1}{p}} \, , \quad (7)$$

with $\sigma_l(\mathcal{H}u(\mathbf{x}))$ the l -th singular value of $\mathcal{H}u(\mathbf{x})$. The above-mentioned regularization functionals named Hessian variation (HV) favor vanishing second-order differentials, hence lead to piecewise-linear reconstructions in comparison with piecewise-constant reconstructions produced by total variation. They allow not only to prevent the undesired staircasing effect but also to provide better approximation of the spatial variation of image intensities.

In spite of the effectiveness of these Hessian-based regularizers, there are however few important characteristics of fluorescence imaging which were not considered by this approach, especially the sparsity of the spatial distribution of high-intensity regions and the colocalization between these regions and those with high magnitude gradients. In the next part, we introduce a novel regularization approach which exploits these interesting characteristics but preserves the desired properties of total variation as well as Hessian variation, such as convexity, contrast, rotation, translation, and scale invariance. It enables thus the application of convex optimization algorithms that are very efficient for large scale problems as in the context of fluorescence microscopy.

3.2 Generalized sparse variation

Originally introduced in [1] for brain MRI segmentation, sparse variation (SV) is a non-quadratic penalty defined as

$$SV_\rho(u) = \int_{\Omega} \underbrace{\sqrt{\rho^2 \|\nabla u(\mathbf{x})\|_2^2 + (1 - \rho)^2 u(\mathbf{x})^2}}_{\|K_{1,\rho} u\|_2} d\mathbf{x} , \quad (8)$$

where $\rho \in]0, 1[$ is a parameter controlling the trade-off between spatial regularity and sparsity, and $K_{1,\rho}$ is the linear operator gathering the image gradient and the image intensity components :

$$K_{1,\rho} = \begin{bmatrix} (1 - \rho) \text{Id} \\ \rho \nabla \end{bmatrix} \text{ and } K_{1,\rho} u(\mathbf{x}) = \begin{pmatrix} (1 - \rho)u(\mathbf{x}) \\ \rho \partial_x u(\mathbf{x}) \\ \rho \partial_y u(\mathbf{x}) \end{pmatrix} \in \mathbb{R}^3 , \quad (9)$$

with ∂_x and ∂_y denote the first order derivative in the horizontal and vertical direction respectively. From this point-of-view, sparse variation is closely similar to total variation and can also be expressed as a mixed L_1 - L_2 norm as :

$$SV_\rho(u) = \|K_{1,\rho} u\|_{1,2} , \quad (10)$$

where the operator $K_{1,\rho}$ is considered instead of the gradient operator. This regularizer has been proposed to reduce blocking artifacts by combining the L_1 penalty (on the image intensity), which enforces the sparsity of the images with TV penalty, which enforces the sparsity of image gradient. The idea behind this combination is to sparsify jointly the spatial distribution of image intensities and image gradients and to allow smooth variations between spatially-contiguous non-zero regions of the underlying image. Indeed, it encourages images with background with small intensity values and sparsely distributed bright objects since if a pixel is non-null, the gradient vector at this pixel is non-null as well, or otherwise both of them are null. Such images look like surprisingly to those which are typically obtained in fluorescence imaging.

Based on the concept of grouping image intensity and spatial differentials, we propose an extended version of sparse variation using the second order differentiation operator. The proposed regularization which is named as Hessian-based sparse variation (HSV) is defined as the following :

$$HSV_\rho(u) = \int_{\Omega} \sqrt{\rho^2 \|\mathcal{H}u(\mathbf{x})\|_F^2 + (1 - \rho)^2 u(\mathbf{x})^2} d\mathbf{x} , \quad (11)$$

where $\|\cdot\|_F$ denotes for the matrix Frobenius norm and $\rho \in]0, 1[$ is the weighting parameter. We also note that the Frobenius norm which is the square root of the sum of squared matrix entries coincides with the Schatten 2-norm ($\|\cdot\|_{\mathcal{S}_2}$) in the case of the Hessian matrix due to its symmetry. More interestingly, by using the fact that the Frobenius norm of the Hessian matrix is equal to the Euclidean norm of its vectorized version, if we define

$$K_{2,\rho} \triangleq \begin{bmatrix} (1 - \rho) \text{Id} \\ \rho \partial_{xx}^2 \\ \rho \partial_{xy}^2 \\ \rho \partial_{yx}^2 \\ \rho \partial_{yy}^2 \end{bmatrix} , \quad (12)$$

the expression of the Hessian-based sparse variation can be re-written as :

$$HSV_\rho(u) = \int_{\Omega} \|K_{2,\rho} u\|_2 d\mathbf{x} = \|K_{2,\rho} u\|_{1,2} . \quad (13)$$

It recalls once again the famous mixed L_1 - L_2 norm mentioned earlier. Our Hessian-based regularization is analogous to those introduced in [20] which also combines image intensities and second-order differentials but a relaxed logarithm function is used for more sparsifying effect as

$$u \mapsto \int_{\Omega} \log(\|K_{2,\frac{1}{2}} u\|_2 + \varepsilon^2) \, d\mathbf{x} \, , \quad (14)$$

where $\varepsilon > 0$ is a control parameter to prevent the singularity at 0 of the logarithm.

From the definitions (8)–(13), we remark furthermore that the original sparse variation and its Hessian-based version correspond to convex regularizers since they are defined as the integration of linear operators. It is easy to verify that these regularizers are homogeneous, shift- and rotation-invariant as total variation. These properties not only are important in the sense of mathematical functional analysis but also allow the design of exact and efficient algorithms which are not possible for the smooth logarithm-based regularizer described in [20]. In general, by using an arbitrary k -th order differentiation operator and by replacing the L_1 -norm by a L_ν -norm ($\nu \geq 1$), we obtain a generalized version of sparse variation as the following :

$$\begin{aligned} \text{GSV}_{\rho,\nu}^{(k)}(u) &\triangleq \|K_{k,\rho} u\|_{\nu,2}^\nu \\ &\triangleq \int_{\Omega} \left[\rho^2 \|\mathcal{D}^{(k)} u(\mathbf{x})\|_2^2 + (1 - \rho)^2 u(\mathbf{x})^2 \right]^{\frac{\nu}{2}} d\mathbf{x} \, , \end{aligned} \quad (15)$$

where $\mathcal{D}^{(k)}$ denotes the corresponding vectorized version of a k -th order differentiation operator and ν is the parameter controlling the convexity degree of the functional. The family of convex regularizers $\text{GSV}_{\rho,\nu}^{(k)}$ includes therefore sparse variation ($k = 1, \nu = 1$) and Hessian-based sparse variation ($k = 2, \nu = 1$). In this work, we only consider $k = 1$ or 2 for the sake of simplicity, and we focus on the case of $\nu = 1$ to impose the sparsity of the image transform $K_{k,\rho} u$ which is the most important property to restore fluorescence images.

4 Variational image deconvolution

4.1 Continuous framework

Given an observed image $f : \Omega \rightarrow \mathbb{R}$ which is blurred and noisy, image deconvolution consists in restoring the underlying image $u : \Omega \rightarrow \mathbb{R}$ such that the following acquisition model holds :

$$f = \mathcal{T}(Hu) \, , \quad (16)$$

where H denotes the linear operator representing the blur related to the optical system (*e.g.*, point spread function) and \mathcal{T} is a degradation operator modeling the measurement noise. In fluorescence microscopy, the arising shot noise is usually modeled by the Poisson distribution (or eventually by a mixed Poisson-Gaussian distribution) which is non-stationary and signal-dependent. Although this model is very convenient for modeling purpose, it also leads to practical computational difficulties since its associated data fidelity term is non-quadratic and is defined only for strictly positive images (not defined for images having zero-value pixels). To avoid the strict positivity issue, instead of considering the Poisson noise model, we assume, in this work, that the observed image f is corrupted by a Gaussian white noise as the following :

$$f = Hu + \eta \, , \quad (17)$$

where η denotes the additive Gaussian noise with zero-mean and standard deviation σ . Variance stabilization techniques [22, 32, 33, 34] can be used in the case of Poisson-Gaussian noise to approximately convert the mixed noise into a Gaussian noise [35].

Under the assumption of additive Gaussian noise, the associated data fidelity term is a quadratic functional which corresponds to a least-squares fitting :

$$E_D(u) = \frac{1}{2} \int_{\Omega} (Hu(\mathbf{x}) - f(\mathbf{x}))^2 d\mathbf{x} . \quad (18)$$

Putting together this quadratic data term and the proposed regularization, the so-called SV (sparse variation) deconvolution can be reformulated as a minimization problem :

$$\begin{aligned} \hat{u} &= \arg \min_u \frac{1}{2} \|Hu - f\|_2^2 + \lambda \|K_{k,\rho} u\|_{1,2} \\ &= \arg \min_u \int_{\Omega} \left[\frac{1}{2} (Hu(\mathbf{x}) - f(\mathbf{x}))^2 + \lambda \|K_{k,\rho} u(\mathbf{x})\|_2 \right] d\mathbf{x} , \end{aligned} \quad (19)$$

where $k = 1$ or 2 , $0 \leq \rho \leq 1$ and $\lambda \geq 0$ is the regularization parameter. We remark that the problem (19) is convex since the underlying energy functional is sum of convex terms, but it is non-smooth because of the singularity of the regularization term. Solving such a problem is not a trivial task due to its non-smoothness. Smooth approximation can be envisaged to overcome the non-differentiability of the underlying energy functional (objective) if we want to use standard differentiable optimization techniques (such as gradient descent or Newton-Raphson method). However, the solution of the approximated problem could be different from those of the original problem because the behavior of the objective is modified. Up to our knowledge, only primal-dual methods [36, 37] allows to solve directly this kind of convex and non-smooth problem without any modification of the energy functional.

4.2 Discrete formulation

Since the observed noisy and blurry image f , which is obtained at the end of the acquisition process, is represented by its digitized (discrete) version and not by its continuously defined counterpart. The continuous model is not appropriate for discrete images even though the estimation of the continuous image u from discrete samples of f is in principle possible. For that reason, we propose to consider a discrete version of (19) by assuming that the images u and f are sampled according to the sampling grid

$$\Lambda = \mathbb{Z}^2 \cap \Omega = \{1, 2, \dots, M\} \times \{1, 2, \dots, N\} . \quad (20)$$

For a coordinate $\mathbf{p} = (i, j) \in \Lambda$, we denote by $u_{i,j} = u(\mathbf{p})$ (resp. $f_{i,j} = f(\mathbf{p})$) the value of u (resp. f) at the position (i, j) . Discrete version of these images are therefore given by $\{u_{i,j}\}_{1 \leq i \leq M, 1 \leq j \leq N}$ and $\{f_{i,j}\}_{1 \leq i \leq M, 1 \leq j \leq N}$. Let us consider $\mathcal{X} = \mathbb{R}^{MN}$ a finite dimensional vector space equipped with a standard inner (scalar) product

$$\langle w, w' \rangle_{\mathcal{X}} = \sum_{i=1}^M \sum_{j=1}^N w_{i,j} w'_{i,j} . \quad (21)$$

The induced norm by the defined inner product is given by

$$\|w\|_{\mathcal{X}_2} = \sqrt{\langle w, w \rangle_{\mathcal{X}}} = \left(\sum_{i=1}^M \sum_{j=1}^N w_{i,j}^2 \right)^{\frac{1}{2}} . \quad (22)$$

It is easy to check that both $\{u_{i,j}\}_{i,j}$ and $\{f_{i,j}\}_{i,j}$ belong to the mentioned vector space \mathcal{X} .

In the following, without risk of ambiguity, we will consider the notations $K_{k,\rho} : \mathcal{X} \rightarrow \mathcal{X}^{2^k+1}$ and $H : \mathcal{X} \rightarrow \mathcal{X}$ for discrete versions associated with the intensity-differential-grouping and the blurring operator. In the discrete setting, the blurring operator H corresponds to a discrete convolution which can be efficiently computed by using fast Fourier transform (FFT) [38, 39, 40, 41]. To discretize $K_{k,\rho}$ (with $k = 1$ or 2), we use standard finite differences for the gradient and Hessian operators with Neumann conditions on image boundaries

$$(K_{1,\rho}u)_{i,j} = \begin{pmatrix} (1-\rho)u_{i,j} \\ \rho(D_1^{(1)}u)_{i,j} \\ \rho(D_2^{(1)}u)_{i,j} \end{pmatrix} \in \mathbb{R}^3, \quad (23)$$

and

$$(K_{2,\rho}u)_{i,j} = \begin{pmatrix} (1-\rho)u_{i,j} \\ \rho(D_{1,1}^{(2)}u)_{i,j} \\ \rho(D_{1,2}^{(2)}u)_{i,j} \\ \rho(D_{2,1}^{(2)}u)_{i,j} \\ \rho(D_{2,2}^{(2)}u)_{i,j} \end{pmatrix} \in \mathbb{R}^5, \quad (24)$$

where

$$(D_1^{(1)}u)_{i,j} = \begin{cases} u_{i+1,j} - u_{i,j} & \text{if } i < M, \\ 0 & \text{if } i = M, \end{cases} \quad (25a)$$

$$(D_2^{(1)}u)_{i,j} = \begin{cases} u_{i,j+1} - u_{i,j} & \text{if } j < N, \\ 0 & \text{if } j = N, \end{cases} \quad (25b)$$

$$(D_{1,1}^{(2)}u)_{i,j} = \begin{cases} u_{i+1,j} - 2u_{i,j} - u_{i-1,j} & \text{if } 1 < i < M, \\ 0 & \text{otherwise} \end{cases}, \quad (25c)$$

$$(D_{2,2}^{(2)}u)_{i,j} = \begin{cases} u_{i,j+1} - 2u_{i,j} - u_{i,j-1} & \text{if } 1 < j < N, \\ 0 & \text{otherwise} \end{cases}, \quad (25d)$$

$$(D_{1,2}^{(2)}u)_{i,j} = (D_{2,1}^{(2)}u)_{i,j} = \begin{cases} u_{i+1,j+1} - u_{i+1,j} - u_{i,j+1} + u_{i,j} & \text{if } i < M \text{ and } j < N, \\ 0 & \text{otherwise} \end{cases}. \quad (25e)$$

Let us consider these discrete operators and define the mixed L_1 - L_2 norm of $\{(K_{k,\rho}u)_{i,j}\}_{i,j}$ as

$$\|K_{k,\rho}u\|_{\mathcal{X}_{1,2}} = \sum_{i=1}^M \sum_{j=1}^N \|(K_{k,\rho}u)_{i,j}\|_2, \quad (26)$$

where the L_1 -norm acts now on the discrete domain Λ . The energy functional associated with SV deconvolution problem in the discrete setting then reads, where $\lambda \geq 0$,

$$E(u) = \frac{1}{2} \|Hu - f\|_{\mathcal{X}_2}^2 + \lambda \|K_{2,\rho}u\|_{\mathcal{X}_{1,2}}. \quad (27)$$

Furthermore, due to the nature of photon-limited imaging in fluorescence microscopy which implies that image intensities are upper and lower bounded, range constraints on image intensities can also be added

$$\begin{aligned} \mathcal{C} &= \{u : 0 \leq u_{i,j} \leq u_{\max}, 1 \leq i \leq M, 1 \leq j \leq N\} \\ &= [0, u_{\max}]^{MN} \subset \mathcal{X}, \end{aligned} \quad (28)$$

where the lower bound 0 guarantees to positivity of the solution and the upper bound $u_{\max} > 0$ is the maximal intensity value allowed. Finally, we consider the following minimization problem :

$$\hat{u} = \arg \min_u \frac{1}{2} \|Hu - f\|_{\mathcal{X}_2}^2 + \lambda \|K_{k,\rho} u\|_{\mathcal{X}_{1,2}} + \iota_{\mathcal{C}}(u) , \quad (29)$$

where $\iota_{\mathcal{C}}$ denotes the characteristic function of the convex subset \mathcal{C} defined as

$$\iota_{\mathcal{C}}(u) = \begin{cases} 0 & \text{if } u \in \mathcal{C} , \\ +\infty & \text{otherwise} . \end{cases} \quad (30)$$

We notice that the objective function in (29) is a sum of linear composite functions as $u \mapsto \sum_{n=1}^m \mathcal{F}_n(L_n u)$, where each \mathcal{F}_n is a convex function and each L_n is a linear bounded operator. Formally, we can write $m = 3$, $\mathcal{F}_1 = \iota_{\mathcal{C}}$, $L_1 = \text{Id}$, $\mathcal{F}_2 = \lambda \|\cdot\|_{\mathcal{X}_{1,2}}$, $L_2 = K_{k,\rho}$ and $\mathcal{F}_3 = \frac{1}{2} \|\cdot\|_{\mathcal{X}_2}^2$, $L_3 = H(\cdot) - f$. Generic primal-dual proximal approaches can be used to minimize this linear combination of convex functions as proposed in [42, 43], but it is not optimal since the smoothness of the quadratic terms $\frac{1}{2} \|Hu - f\|_{\mathcal{X}_2}^2$ is not exploited. In order to solve the problem (29), the design of an appropriate algorithm requires therefore to take into account the specific form of the corresponding energy, *i.e.* the sum of a simple convex function $\mathcal{F} = \iota_{\mathcal{C}}$, a more sophisticated composite function $\mathcal{G} \circ L = \lambda \|K_{k,\rho}(\cdot)\|_{\mathcal{X}_{1,2}}$ (here, $\mathcal{G} = \lambda \|\cdot\|_{\mathcal{X}_{1,2}}$ and $L = K_{k,\rho}$) and a smooth function $\mathcal{H} = \frac{1}{2} \|H(\cdot) - f\|_{\mathcal{X}_2}^2$.

4.3 Minimization of the proposed energy

In this section, we present a first-order method to minimize the sum of convex functions in (29), based on the proximal splitting approaches [44, 45, 46, 47, 48, 36, 37, 49]. It consists in decomposing (splitting) the original problem into several simple sub-problems in the way that each single function of the sum can be processed separately. Indeed, smooth function involves its gradient operator, while non-smooth function implies its Moreau proximity operator [50]. These operators are well-suited for large-scale problems arising in signal and image processing, because they only exploit first-order information of the function and thus enable fast and efficient computation.

Let us recall first that the proximity operator of a convex function $\mathcal{J} : \mathcal{X} \rightarrow \mathbb{R}$ is defined as

$$\text{prox}_{\tau \mathcal{J}}(u) = \arg \min_{w \in \mathcal{X}} \mathcal{J}(w) + \frac{1}{2\tau} \|u - w\|_{\mathcal{X}_2}^2 , \quad (31)$$

where $\tau > 0$ is a control parameter. From this definition, it easy to verify that the proximity operator of the function $\mathcal{F}(u) = \iota_{\mathcal{C}}(u)$ is nothing else than the projection (according to the norm $\|\cdot\|_{\mathcal{X}_2}$) onto the convex subset $\mathcal{C} = [0, u_{\max}]^{MN}$ as the following

$$\begin{aligned} \text{prox}_{\tau \mathcal{F}}(u) &= \arg \min_{w \in \mathcal{X}} \iota_{\mathcal{C}}(w) + \frac{1}{2\tau} \|u - w\|_{\mathcal{X}_2}^2 \\ &= \arg \min_{w \in \mathcal{C}} \|u - w\|_{\mathcal{X}_2}^2 . \end{aligned} \quad (32)$$

If we denote $\text{proj}_{\mathcal{C}}$ the projection operator on \mathcal{C} , its closed-form expression is given by

$$(\text{proj}_{\mathcal{C}}(u))_{i,j} = \max(0, \min(u_{\max}, u_{i,j})) , \quad (33)$$

which is completely simple and easy to compute. Meanwhile, the quadratic function $\mathcal{H}(u) = \frac{1}{2} \|Hu - f\|_{\mathcal{X}_2}^2$ possesses an analytic form for its associated proximity operator but the latter is

slightly complicated

$$\begin{aligned}\text{prox}_{\tau\mathcal{H}}(u) &= \arg \min_{w \in \mathcal{X}} \frac{1}{2} \|Hw - f\|_{\mathcal{X}_2}^2 + \frac{1}{2\tau} \|u - w\|_{\mathcal{X}_2}^2 \\ &= (\tau H^\top H + \text{Id})^{-1} (\tau H^\top H f + u) ,\end{aligned}\tag{34}$$

where the symbol $^\top$ denotes the adjoint of a linear operator and $H^\top : \mathcal{X} \rightarrow \mathcal{X}$ satisfies $\langle Hw, w' \rangle_{\mathcal{X}} = \langle w, H^\top w' \rangle_{\mathcal{X}}$. The evaluation of $\text{prox}_{\tau\mathcal{H}}(u)$ corresponds to the inverse of a linear system that is not always possible in practice due to the high dimension of the problem. For this reason, optimization methods which involve the gradient of \mathcal{H} are more appropriate since they do not require any inverse operator. In the comparison with \mathcal{F} and \mathcal{H} , the calculation of the proximity operator in the case of the composite function $\mathcal{G} \circ L(u) = \lambda \|K_{k,\rho} u\|_{\mathcal{X}_{1,2}}$ is theoretically possible but is challenging because of the presence of $K_{k,\rho}$ which is not diagonal.

To solve the minimization problem (29), we adopt the full splitting approach described in [37, 49]. The key idea of this approach is to evaluate the gradient, proximity and linear operators individually in order to avoid implicit operations such as inner loops or inverse of linear operators. Accordingly, only “simple” computations are considered such as the gradient $\nabla \mathcal{H}$, the proximity operators of \mathcal{F} and \mathcal{G} , the linear mapping L and its adjoint operators L^\top . The corresponding proximal algorithm for the problem (29) is written under the following general form :

$$u^{(\ell+1)} = \text{prox}_{\gamma\mathcal{F}} \left\{ u^{(\ell)} - \gamma \left(L^\top z^{(\ell)} + \nabla \mathcal{H}(u^{(\ell)}) \right) \right\},\tag{35a}$$

$$z^{(\ell+1)} = \text{prox}_{\zeta\mathcal{G}^*} \left\{ z^{(\ell)} + \zeta L \left(2u^{(\ell+1)} - u^{(\ell)} \right) \right\},\tag{35b}$$

where $\gamma, \zeta > 0$ are proximal parameters, \mathcal{G}^* denotes the Legendre-Fenchel conjugate of \mathcal{G} and its proximity operator $\text{prox}_{\zeta\mathcal{G}^*}$ can be directly computed from $\text{prox}_{\frac{\mathcal{G}}{\zeta}}$ by using Moreau’s identity $v = \zeta \text{prox}_{\frac{\mathcal{G}}{\zeta}}(\frac{v}{\zeta}) + \text{prox}_{\zeta\mathcal{G}^*}(v)$. Following [37, 49], to guarantee the convergence of the proposed algorithm, the parameters γ and ζ must fulfill the condition

$$\gamma \left(\frac{1}{2} + \zeta \|L^\top L\| \right) < 1 ,\tag{36}$$

where $\|\cdot\|$ denotes the operator norm. The proofs of the convergence can be found in [37]. We also note that the proposed algorithm belongs to the class of primal-dual algorithms which provide not only the solution of the primal problem (*a.k.a.* the original minimization problem) but also the solution of its dual problem.

Since the closed-form of $\text{prox}_{\gamma\mathcal{F}}$ is already given, it remains us now to define the analytic expression of other terms in (35a) and (35b). We start with the gradient of the quadratic function \mathcal{H} which is straightforwardly obtained by

$$\nabla \mathcal{H}(u) = H^\top (Hu - f) .\tag{37}$$

Next, we remark that the regularization operator $L = K_{k,\rho}$ is a linear mapping $u \in \mathcal{X} \mapsto K_{k,\rho} u = (v^t)_{1 \leq t \leq 2^k+1} \in \mathcal{X}^{2^k+1}$, then its adjoint operator $L^\top = K_{k,\rho}^\top$ is defined using the equation $\langle u, K_{k,\rho}^\top v \rangle_{\mathcal{X}} = \langle K_{k,\rho} u, v \rangle_{\mathcal{X}^{2^k+1}}$, which implies

$$(K_{1,\rho}^\top v)_{i,j} = (1 - \rho) v_{i,j}^1 + \rho [(D_1^{(1)})^\top v^2]_{i,j} + \rho [(D_2^{(1)})^\top v^3]_{i,j}\tag{38}$$

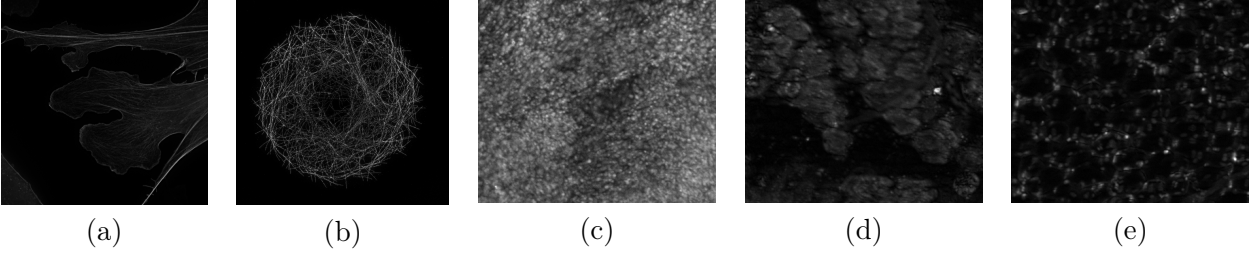


FIGURE 1 – **Set of biological images acquired by SIM technology.** From left to right : (a) actin cytoskeleton, (b) microtubule, (c) tumor tissue, (d) muscle tissue, and (e) adipose tissue. The first two images are cell images collected from the Cell Image Library (<http://www.cellimagelibrary.org>) with id number CIL 7053 and CIL 36147 respectively (CIL stands for the Cell Image Library identifier). The last three images are tissue images in the dataset used in [51] (available at <https://dukespace.lib.duke.edu/dspace/handle/10161/10892>).

and

$$\begin{aligned} (K_{2,\rho}^\top v)_{i,j} = & (1 - \rho)v_{i,j}^1 + \rho[(D_{1,1}^{(2)})^\top v^2]_{i,j} + \rho[(D_{1,2}^{(2)})^\top v^3]_{i,j} \\ & + \rho[(D_{2,1}^{(2)})^\top v^4]_{i,j} + \rho[(D_{2,2}^{(2)})^\top v^5]_{i,j} , \end{aligned} \quad (39)$$

where the involving adjoint operators $(D_1^{(1)})^\top$, $(D_2^{(1)})^\top$, $(D_{1,1}^{(2)})^\top$, $(D_{1,2}^{(2)})^\top$, $(D_{2,1}^{(2)})^\top$, and $(D_{2,2}^{(2)})^\top$ are given in the appendix section. From equations (38) and (39), one can deduce the following upper bounds :

$$\|K_{1,\rho}^\top K_{1,\rho}\| \leq (1 - \rho)^2 + 8\rho^2 , \quad (40a)$$

$$\|K_{2,\rho}^\top K_{2,\rho}\| \leq (1 - \rho)^2 + 64\rho^2 , \quad (40b)$$

that are used for choosing the proximal parameters γ and ζ .

The last term we want to deal with is the proximity operator $\text{prox}_{\zeta\mathcal{G}^*}$. We also note that the proposed primal-dual algorithm does not necessitate evaluating the proximity operator of the composite function $\mathcal{G} \circ L$ as in the case of generic proximal algorithms, but only $\text{prox}_{\frac{\mathcal{G}}{\zeta}}$ is required. Since \mathcal{G} is related to the mixed L_1 - L_2 norm $\|\cdot\|_{\mathcal{X}_{1,2}}$ whose the proximity operator is defined as :

$$(\text{prox}_{\tau\|\cdot\|_{\mathcal{X}_{1,2}}}(v))_{i,j}^t = \max(0, \|L_{i,j}v\|_2 - \tau) \frac{v_{i,j}^t}{\|L_{i,j}v\|_2} , \quad (41)$$

where $L_{i,j} : v \in \mathcal{X}^{2^k+1} \mapsto (v_{i,j}^t)_{1 \leq t \leq 2^k+1} \in \mathbb{R}^{2^k+1}$ is a linear operator ; by using the Moreau's identity, we obtain the closed-form expression of $\text{prox}_{\zeta\mathcal{G}^*}$ as the following :

$$(\text{prox}_{\zeta\mathcal{G}^*}(v))_{i,j}^t = \frac{v_{i,j}^t}{\max\left(1, \frac{\|L_{i,j}v\|_2}{\lambda}\right)} , \quad (42)$$

which shows that $\text{prox}_{\zeta\mathcal{G}^*}$ is independent from ζ and moreover it is an pointwise operator. These properties allow therefore fast and efficient computation by exploiting the intrinsic parallelism of multicore processors.

TABLE 1 – Properties of regularizers which are used in the deconvolution experiments.

Regularizer	Differentiation order	Convexity	Smoothness
Total Variation (TV)	1	Convex	Non smooth
Hessian Variation (HV)	2	Convex	Non smooth
TV- L_1	1	Convex	Non smooth
GraphNet (GN)	1	Convex	Non smooth
Sparse Variation (SV)	1	Convex	Non smooth
Hessian-based SV (HSV)	2	Convex	Non smooth
TV Huber (TVH)	1	Convex	Smooth
HV Huber (HVH)	2	Convex	Smooth
TV- L_1 Huber (TV- L_1 H)	1	Convex	Smooth
HV- L_1	2	Convex	Non smooth
HV- L_1 Huber (HV- L_1 H)	2	Convex	Smooth
GraphNet Huber (GNH)	1	Convex	Smooth
Hessian-based GN (HGN)	2	Convex	Non smooth
HGN Huber (HGNH)	2	Convex	Smooth
SV Huber (SVH)	1	Convex	Smooth
HSV Huber (HSVH)	2	Convex	Smooth
Arigovindan <i>et al.</i> [20] (LHSV)	2	Non convex	Smooth

5 Experimental results

To evaluate the performance of the sparse variation (SV) deconvolution approach, we provide experimental comparisons with classical deconvolution methods [52], that are commonly used in fluorescence microscopy such as the Richardson-Lucy (RL) algorithm, the iterative constrained Tikhonov-Miller (ICTM) algorithm, and the Gold-Meinell (GM) algorithm, and with recent regularization-based deconvolution methods, including total variation (TV), Hessian variation (HV), GraphNet (GN) [53, 54, 55], TV- L_1 [56, 57], and specially the non-convex regularizer (14) introduced by Arigovindan *et al.* [20]. The latter involves second order differentiation operator and is based on the logarithm function. It is abbreviated as LHSV (Log-based Hessian Sparse Variation) due to its similarity with the concept of SV. We recall that GraphNet is the sum of the L_1 norm of the image intensity and the squared L_2 norm of the image gradient (*i.e.* the Tikhonov penalty), whereas TV- L_1 differs from GraphNet by replacing the Tikhonov penalty by TV penalty :

$$\text{GN}_\rho(u) = \rho \|\nabla u\|_2^2 + (1 - \rho) \|u\|_1 , \quad (43)$$

$$\text{TVL1}_\rho(u) = \rho \|\nabla u\|_{1,2} + (1 - \rho) \|u\|_1 . \quad (44)$$

To enrich the catalog of convex regularizers used in these experiments, by using the Hessian operator instead of the gradient operator, we consider also an extended version of GraphNet and TV- L_1 which can be named as Hessian-based GraphNet (HGN) and Hessian Variation- L_1 (HV- L_1) respectively. Furthermore, Huber-norm-based smooth approximations of non-smooth regularization functionals, which enable the use of smooth optimization techniques such as gradient-descent-based methods, are also considered in our study. For these smooth regularization functionals, we use the projected gradient method to minimize the underlying deconvolution energy. In contrast, a full-splitting-based primal-dual algorithm [37, 49] is used in the case of non-smooth regularization functionals.

One important motivation of this work was to investigate the impact of smooth and non-smooth regularizers for image deconvolution. In Table 1, we summarize the characteristics of the regularizers mentioned above. The deconvolution experiments were performed on an image set composed of both synthetic and real fluorescence images depicting bright objects over dark backgrounds.

TABLE 2 – Information of test images (see Fig. 1).

Image	Type	Image size	Pixel size	Spatial resolution
Actin cytoskeleton	Cell	1904×1900 px	$0.04 \mu m$	$0.1 \mu m$
Microtubule	Cell	1054×1028 px	$0.04 \mu m$	$0.1 \mu m$
Tumor	Tissue	350×300 px	$1.50 \mu m$	$4.4 \mu m$
Muscle	Tissue	350×300 px	$1.50 \mu m$	$4.4 \mu m$
Adipose	Tissue	350×300 px	$1.50 \mu m$	$4.4 \mu m$

5.1 Experiments on simulated image

We have selected several SIM (Structured Illumination Microscopy) images to serve as blur-free and noise-free reference images (*i.e.* ground-truth) in OUR experiments. SIM imaging allows to reconstruct very fine details at very high resolutions (up to 100 nm for standard SIM techniques) while removing noise from raw acquired measurements. These fluorescence images, shown in Fig. 1, were collected from two sources : the Cell Image Library (CIL) database (available at <http://www.cellimagelibrary.org>) and the training dataset used in [51] for the detection of positive margins in a pre-clinical genetically engineered mouse model of sarcoma. We note that, for the latter data set, the used SIM technique called widefield SIM is specially developed for tissue imaging which does not require sub-cellular resolution. For that reason, the resolution is much more smaller than those of conventional SIM which is approximately 100 nm as in the case of CIL images. In Table 2, we provide detailed information of all test images, including specimen name, image size and spatial resolution.

To produce a homogeneous and fair comparison of different methods and to avoid bias induced by inhomogeneous dynamic ranges between the images, we first normalized the reference images in the range $[0, 1]$ before all further simulations. The normalized images are then blurred by considering a Gaussian point spread function with standard deviation $\sigma_{\text{PSF}} = 2$. A Gaussian noise with zero mean and variance σ^2 is also added to these images in order to generate observed noisy and blurry data. In these experiments, we consider three distinct noise levels corresponding to a standard deviation $\sigma \in \{0.02, 0.04, 0.08\}$ respectively. Quantitative evaluation of each deconvolution method is measured by the Peak Signal-to-Noise Ratio (PSNR) and by the Structural Similarity (SSIM) index between the deconvolved images and the reference images.

For regularization-based methods which combine penalties on image intensity and on image differentiation operator (such as SV, TV- L_1 , GraphNet and their variants), we set the trade-off parameter $\rho = 0.5$, implying the equal contribution of each component for simplification purpose. In the case of the Richardson-Lucy (RL) algorithm which is originally designed to deal with Poisson noise, the degraded images are re-scaled to the original dynamics of the underlying reference images by multiplying by a normalization factor. The RL deconvolution results are then re-normalized for a fair comparison with those obtained by the other methods. Before applying the Gold-Meinl algorithm, the noisy images are smoothed with a Gaussian filter as pre-processing step because this algorithm assumes that the noise is negligible.

Quantitative evaluation

In Table 3, we provide the comparative results of the proposed SV deconvolution with the tested methods for the set of fluorescence images shown in Fig. 1, for different degradation conditions. Note that the deconvolution outcome of each method was obtained using parameters which were tuned in the way that produce the best PSNR performance. Using these fine-tuned parameters, the SSIM

TABLE 3 – Performance of considered deconvolution methods in terms of PSNR and SSIM on the set of biomedical test images for three different noise levels.

Image	Actin cytoskeleton			Microtubule			Tumor			Muscle			Adipose		
	$\sigma=0.02$	$\sigma=0.04$	$\sigma=0.08$	$\sigma=0.02$	$\sigma=0.04$	$\sigma=0.08$	$\sigma=0.02$	$\sigma=0.04$	$\sigma=0.08$	$\sigma=0.02$	$\sigma=0.04$	$\sigma=0.08$	$\sigma=0.02$	$\sigma=0.04$	$\sigma=0.08$
PSNR	RL	-3.87	-3.88	-3.92	27.89	23.11	17.86	22.77	17.66	27.67	22.37	17.15	26.02	21.25	15.65
	ICTM	35.77	34.39	32.65	29.28	27.98	26.61	26.07	24.53	34.19	32.74	31.14	33.74	31.98	30.17
	GM	-4.02	-4.03	-4.05	28.92	24.82	19.79	24.15	18.80	29.26	23.94	18.51	27.12	22.85	17.42
	TV	35.46	34.32	32.92	29.17	27.88	26.61	25.41	24.05	33.72	32.38	31.14	33.28	31.81	30.17
	TV- L_1	35.45	33.96	31.84	29.25	27.93	26.62	25.40	23.94	33.67	32.07	30.13	33.29	31.58	29.45
	GN	33.84	31.15	28.07	29.82	28.26	26.22	25.49	22.83	32.12	29.12	26.07	32.39	29.69	27.08
	SV	35.71	33.41	30.44	30.34	28.82	27.07	25.75	23.31	33.85	31.48	28.72	34.55	32.19	29.37
	HV	36.44	35.20	33.62	29.98	28.57	27.09	26.01	24.41	34.43	32.94	31.43	34.56	32.68	30.63
	HV- L_1	36.36	34.87	32.55	29.99	28.61	27.16	25.99	24.32	34.38	32.67	30.51	34.53	32.54	30.17
	HGN	34.00	31.23	28.09	29.88	28.35	26.32	25.50	22.68	32.33	29.26	26.09	32.66	29.95	27.22
SSIM	HSV	35.71	33.24	30.09	30.42	28.89	27.11	25.70	23.08	33.73	31.21	28.35	34.52	32.14	29.34
	TVH	36.21	34.94	33.32	29.72	28.35	26.94	26.01	24.46	34.35	32.86	31.40	34.22	32.43	30.49
	TV- L_1 H	36.26	34.87	32.85	29.76	28.41	27.03	26.01	24.42	34.33	32.71	30.89	34.22	32.41	30.28
	GNH	33.61	31.43	28.69	28.03	27.45	26.23	25.06	23.09	31.66	29.44	26.78	31.46	29.88	27.75
	SVH	35.88	33.72	30.84	30.13	28.70	27.09	25.83	23.49	34.01	31.74	29.16	34.47	32.37	29.85
	HVH	35.83	34.38	31.97	29.72	28.32	26.87	26.02	24.42	34.16	32.64	30.76	33.84	32.16	30.18
	HV- L_1 H	35.88	34.17	31.33	29.75	28.38	26.98	26.01	24.24	34.14	32.24	29.53	33.87	32.06	29.69
	HGNH	34.55	32.56	29.36	28.28	27.84	26.54	25.52	23.42	32.72	30.57	27.41	32.36	30.67	28.22
	HSVH	35.73	33.65	30.64	29.88	28.47	26.90	25.84	23.65	33.96	31.72	28.88	33.93	31.93	29.42
	LHSV	34.82	32.18	28.11	28.56	27.78	25.47	24.61	20.96	33.23	30.49	26.83	33.93	30.71	27.38
PSNR	RL	0.434	0.432	0.422	0.624	0.363	0.156	0.301	0.128	0.521	0.265	0.102	0.694	0.449	0.201
	ICTM	0.867	0.823	0.765	0.714	0.647	0.586	0.696	0.591	0.840	0.796	0.741	0.859	0.809	0.743
	GM	0.425	0.424	0.418	0.728	0.563	0.370	0.377	0.177	0.610	0.347	0.149	0.745	0.540	0.276
	TV	0.885	0.854	0.815	0.819	0.756	0.677	0.646	0.536	0.830	0.787	0.741	0.866	0.820	0.755
	TV- L_1	0.866	0.792	0.675	0.828	0.778	0.720	0.649	0.546	0.828	0.770	0.677	0.863	0.799	0.680
	GN	0.714	0.608	0.492	0.850	0.795	0.719	0.696	0.576	0.753	0.609	0.436	0.769	0.619	0.453
	SV	0.861	0.790	0.683	0.867	0.819	0.761	0.704	0.596	0.837	0.759	0.632	0.878	0.801	0.668
	HV	0.883	0.846	0.802	0.832	0.765	0.679	0.693	0.581	0.848	0.805	0.750	0.882	0.833	0.765
	HV- L_1	0.869	0.798	0.704	0.837	0.782	0.725	0.692	0.588	0.846	0.792	0.699	0.879	0.816	0.708
	HGN	0.733	0.596	0.468	0.851	0.796	0.717	0.699	0.577	0.764	0.615	0.434	0.785	0.638	0.445
	HSV	0.872	0.797	0.679	0.856	0.818	0.754	0.706	0.594	0.836	0.752	0.612	0.874	0.794	0.661
SSIM	TVH	0.876	0.837	0.790	0.818	0.751	0.665	0.686	0.579	0.846	0.801	0.748	0.875	0.825	0.760
	TV- L_1 H	0.876	0.827	0.761	0.825	0.769	0.706	0.686	0.579	0.846	0.796	0.725	0.873	0.821	0.735
	GNH	0.787	0.690	0.590	0.793	0.769	0.724	0.644	0.560	0.731	0.637	0.501	0.767	0.678	0.555
	SVH	0.876	0.813	0.722	0.846	0.796	0.740	0.701	0.593	0.842	0.771	0.665	0.883	0.821	0.716
	HVH	0.868	0.829	0.737	0.815	0.749	0.645	0.697	0.587	0.841	0.798	0.724	0.865	0.816	0.742
	HV- L_1 H	0.868	0.806	0.706	0.820	0.766	0.717	0.697	0.594	0.841	0.781	0.667	0.864	0.802	0.691
	HGNH	0.823	0.736	0.612	0.804	0.772	0.719	0.662	0.571	0.789	0.696	0.534	0.817	0.717	0.585
	HSVH	0.869	0.801	0.695	0.830	0.773	0.716	0.691	0.579	0.838	0.762	0.637	0.863	0.800	0.680
	LHSV	0.836	0.687	0.528	0.817	0.757	0.587	0.609	0.368	0.804	0.671	0.469	0.847	0.724	0.523

score is computed for an additional quantitative criterion to evaluate the effectiveness of considered deconvolution methods.

According to the results reported in Table 3, we notice that the non-regularization methods such as RL and GM algorithms perform poorly, irrespectively of the images and the noise levels, showing their non-competitiveness when compared with regularization-based methods. The poor performance of these methods is mainly due to the lack of regularization on the solution, leading to noise amplification in deconvolved images. Among the regularization-based methods, the iterative constrained Tikhonov-Miller (ICTM) algorithm, based on the squared L_2 norm of the image gradient, generally produces encouraging results in terms of PSNR and SSIM performance. In some cases, it eventually outperforms other competitors. For example, on the image of tumor tissue (see Fig. 1(c)), ICTM solution achieves the best PSNR and SSIM scores in the case of medium and high noise levels (corresponding to $\sigma = 0.04$ and $\sigma = 0.08$ respectively); meanwhile, slightly inferior scores are obtained for low noise level ($\sigma = 0.02$) but the difference between them and the corresponding highest values is relatively small.

Regarding non-smooth regularizers, Hessian variation consistently gives superior PSNR scores than TV, for all considered images and noise levels. In terms of SSIM performance, it produces better results in most of cases. In comparison to TV that only penalizes image gradient norm, the TV- L_1 approach which introduces additionally the L_1 penalty on image intensities, yields slightly improved PSNR and SSIM values in some few cases. For the remaining cases, the obtained results using TV and TV- L_1 are very similar. The analogous behavior is also noticed when we compare the couple of HV and HV- L_1 regularizers, the second-order extension of TV and TV- L_1 respectively. The experimental results shows furthermore that the second-order regularizers achieve in general higher PSNR and SSIM scores than the corresponding first-order version. In contrast with first-tier performance obtained with these TV-based regularizations, GraphNet and its Hessian-based variant fail to be competitive for many selected images and signal-to-noise ratios. Their PSNR performance falls behind by more than 2 dB in average and even more than 3 dB in some cases, resulting in lower SSIM scores when compared to TV-related approaches that consider non-quadratic penalty on image differential components. Meanwhile, the results provided by sparse variation are almost comparable to those obtained with TV and HV in terms of both PSNR and SSIM performance. Specially, in the case of microtubule image (CIL 36147) which represents sparsely distributed fine filament structures over dark background, SV leaves these two competing regularizers behind on SSIM benchmark, whereas its PSNR score is higher for two noise levels and slightly lower (only 0.02 dB) than HV for the remaining noise level. In contrast to the supremacy of HV with respect to TV, Hessian-based sparse variation, the second-order extension of SV, does not achieve higher performance than its first-order version over half of cases and the difference between results obtained with these two versions are almost insignificant.

Comparing with these convex but non-smooth regularization functionals, the Huber-norm-based approximations yield in general satisfying results. In a few cases, the PSNR and SSIM score are slightly improved by using the smooth approximated version instead of the original counterpart, but slightly inferior performances are also observed in some other cases. More interestingly, the improvement is frequently noticed for first-order regularizers including TV Huber, TV- L_1 Huber, GraphNet Huber and SV Huber, whereas, second-order regularizers usually suffer from a lowering of PSNR score as well as SSIM value. Another smooth regularizer that we wished to investigate is the so-called LHSV which considers a regularization operator gathering the image intensity and the Hessian matrix coefficients as Hessian-based SV, but replaces the square root in the L_2 norm by a smooth approximation of the logarithm. Using the logarithm function enables to enforce the sparsifying effect, LHSV is able to efficiently remove noise in extremely noisy images while preserving

essential details. In our experiments, this sophisticated approach produces however disappointing results on artificially degraded images. Indeed, the PSNR and SSIM scores are barely in the same grade of GraphNet and sharply inferior than those obtained with HV, SV or even TV in most cases.

Visual inspection and assessment

Based on our observations, the PSNR and SSIM benchmark do not yield a consistent ranking on the performance of each deconvolution approach, and thus it is not possible to definitely conclude which method works best among the considered methods. Their effectiveness needs to be assessed visually in local regions. Actually, there are chances that an obtained result with outstanding PSNR and SSIM scores is unacceptable in terms of visual quality, simply due to over-smoothing which results in the loss of fine details in deconvolved images or due to over-sharpening which leads to unrealistic reconstructions. For that reason, we provide in Fig. 2, a comparison showing the example of deconvolution results obtained with different methods on the microtubule image (CIL 36147) degraded by a Gaussian PSF ($\sigma_{\text{PSF}} = 2$) and an additive Gaussian white noise with standard deviation $\sigma = 0.04$. The original image, showing microtubule structures on a *Drosophila S2* cell, was acquired by a Zeiss Elyra Super-resolution microscope equipped with SIM imaging technique and is collected as part of the Marine Biological Laboratory Neurobiology Course in summer 2011.

First, Fig. 2(c) and 2(d) clearly show that the GM and RL algorithms give very poor results. The ICTM algorithm produces, in contrast, more pleasant visual results, but it tends to over-smooth (blur) important structural details in the images (see Fig. 2(e)) due to the quadratic form of the Tikhonov regularizer. Comparing with the blurred ICTM solution, the deconvolved imaged obtained with LHSV has sharper details over an uniform background (see Fig. 2(n)). However, noise is not sufficiently removed, especially in non-background regions. It not only disturbs the visual effect but also makes the detection of fine details more difficult.

Meanwhile, the result provided by TV in Fig. 2(f), is visually unrealistic in spite of its competitive PSNR and SSIM scores against other regularizers. As expected, it suffers from undesirable staircasing effect characterized by sharp edges and contiguous flat regions (also known as piecewise constant image). The staircasing artifacts can be easily observed in bright regions, notably those corresponding to filament structures which represent smooth changes of intensities. A particular consequence of staircasing effect that we want to figure out in the case of TV, is the presence of number of light-shaded spots with constant intensity over relatively darker surrounding areas. Most of these spots correspond generally to high peaks of noise in the blurred image background and do not represent any relevant structure of the original image. A deconvolved image with more homogeneous background is obtained using the TV- L_1 regularization that combines TV with the L_1 norm of the image intensity to prevent pixels having intensity smaller than a certain threshold, and controlled by the weight ρ and the regularization parameter λ . This thresholding which imposes vanishing of low-intensity regions is also known as the feature selection property the TV- L_1 model as reported in [56]. However, this model does not remove staircasing artifacts related to TV regularization. In comparison with the latter, GraphNet addresses both staircasing and light-shaded spot issues by combining the quadratic Tikhonov functional with the L_1 penalty. The deconvolved image has indeed an uniform background (with less light-shaded spots) and a foreground with no apparent contiguous regions of constant intensity, as shown in Fig. 2(h). It is visually more pleasant than TV and TV- L_1 solutions. It however produces slightly blurred image details due to the Tikhonov penalty which promotes smooth changes of intensities. However, it does not suffer from over-smoothing as in the ICTM solution due to the L_1 penalty which prevents nearly-zero intensity pixels, and hence enhances the contrast between bright objects and darker background. This is

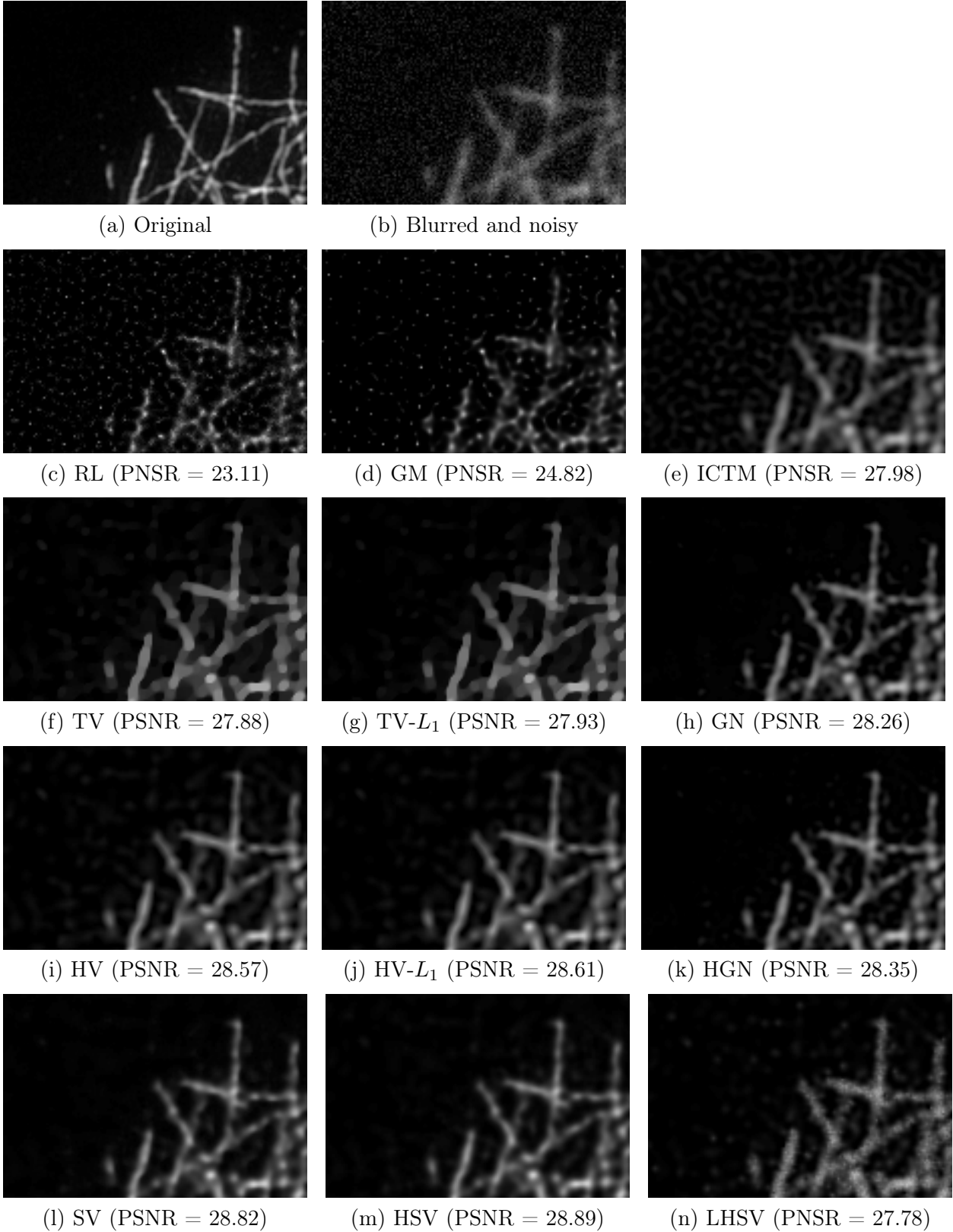


FIGURE 2 – **Deconvolution results on the microtubule image obtained with different methods in comparison to the proposed SV-based approach.** The original image (available at <http://www.cellimagelibrary.org/> with identifier CIL 36147) is degraded by a Gaussian PSF with standard deviation $\sigma_{\text{PSF}} = 2$ and a additive Gaussian noise with zero mean and standard deviation $\sigma = 0.04$. Zoom on filament details is shown in order to compare the performance of each method. The SV and Hessian-based SV solutions are very competitive when compared to those obtained with the other methods.

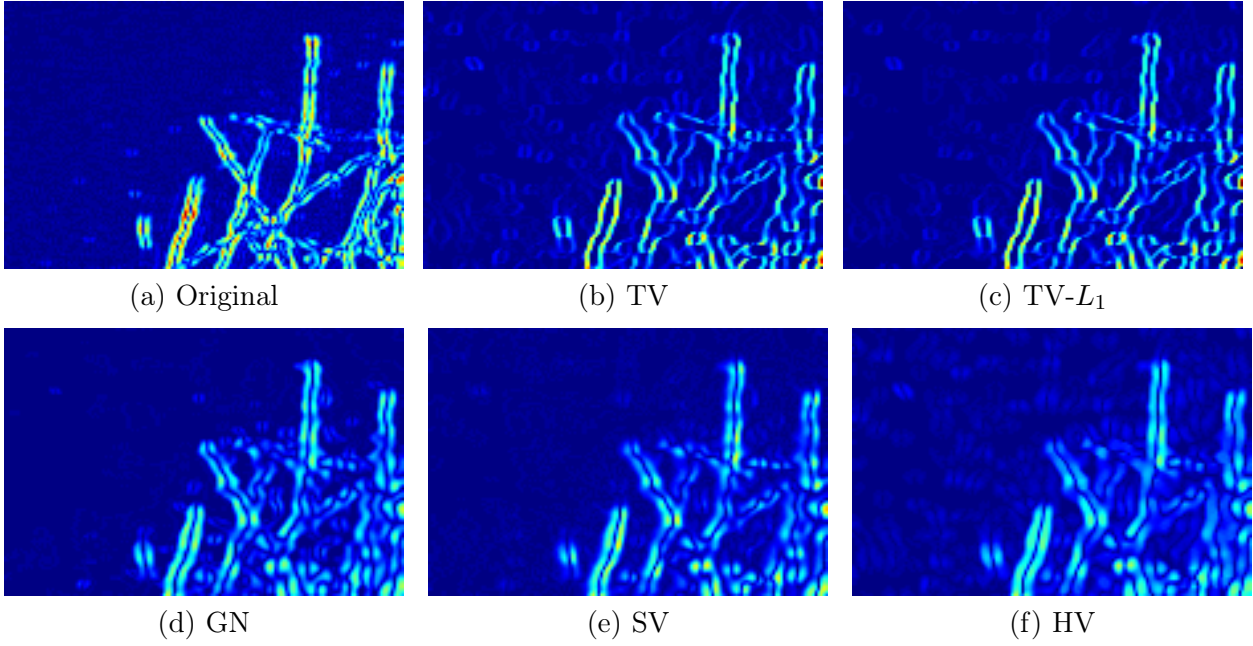


FIGURE 3 – **Gradient magnitude of deconvolution results obtained with several convex regularizers.** The “hot” colors correspond to high gradients and “cold” colors to low gradients.

consistent with the high PSNR and SSIM values. In the particular example of microtubule image, GraphNet outperforms the ICTM, TV and $TV-L_1$ algorithms.

By examining the comparative results reported in Fig. 2, it turns out that SV gives similar results to GraphNet and outperforms all other regularizers which are first-order, convex and non-smooth, in terms of visual quality. The effectiveness of SV approach for fluorescence images, especially in the case of the microtubule image, can be justified by the way that this regularization affects the form of obtained solutions. In contrast with TV (penalty on image gradients), or with $TV-L_1$ and GraphNet that simply sum two penalties acting separately, one on image intensities and the other on image gradients, SV penalizes jointly image intensities and gradients by introducing structured sparsity on a specific linear transform which maps each pixel to an unique vector composed of its intensity and its directional derivatives in order to favor the co-localization of non-zero pixels and gradients. Therefore, it allows to obtain non-zero regions of eventually high-magnitude gradients, in opposition to relatively small-magnitude gradients in the case of GraphNet or vanishing gradients for TV and $TV-L_1$. This behavior results in better reconstruction of the image foreground, in which large intensity variation between pixels at the object boundaries and those in the middle, as well as sharp contrast between different objects may occur, while avoiding undesirable over-smoothing or over-sharpening effect. As an alternative, HV based on the norm of second-order differentiation operator leading to piecewise linear solutions, also permits the reconstruction of high-magnitude gradients not only at the edge of the objects but also inside objects. HV solution shown in Fig. 2(i), is able to restore smooth intensity variations of filament structures and is visually comparable to the GraphNet and SV solutions. The background with some visible light-shaded spots is however non-homogeneous, as expected. Hence, in the example of microtubule image, SV represents so far the best deconvolution result with well-restored fine details and homogeneous background in comparison with existing regularizers including TV, $TV-L_1$, GraphNet and HV.

To better appreciate the behavior of the regularization approaches, Fig. 3 depicts the gradient

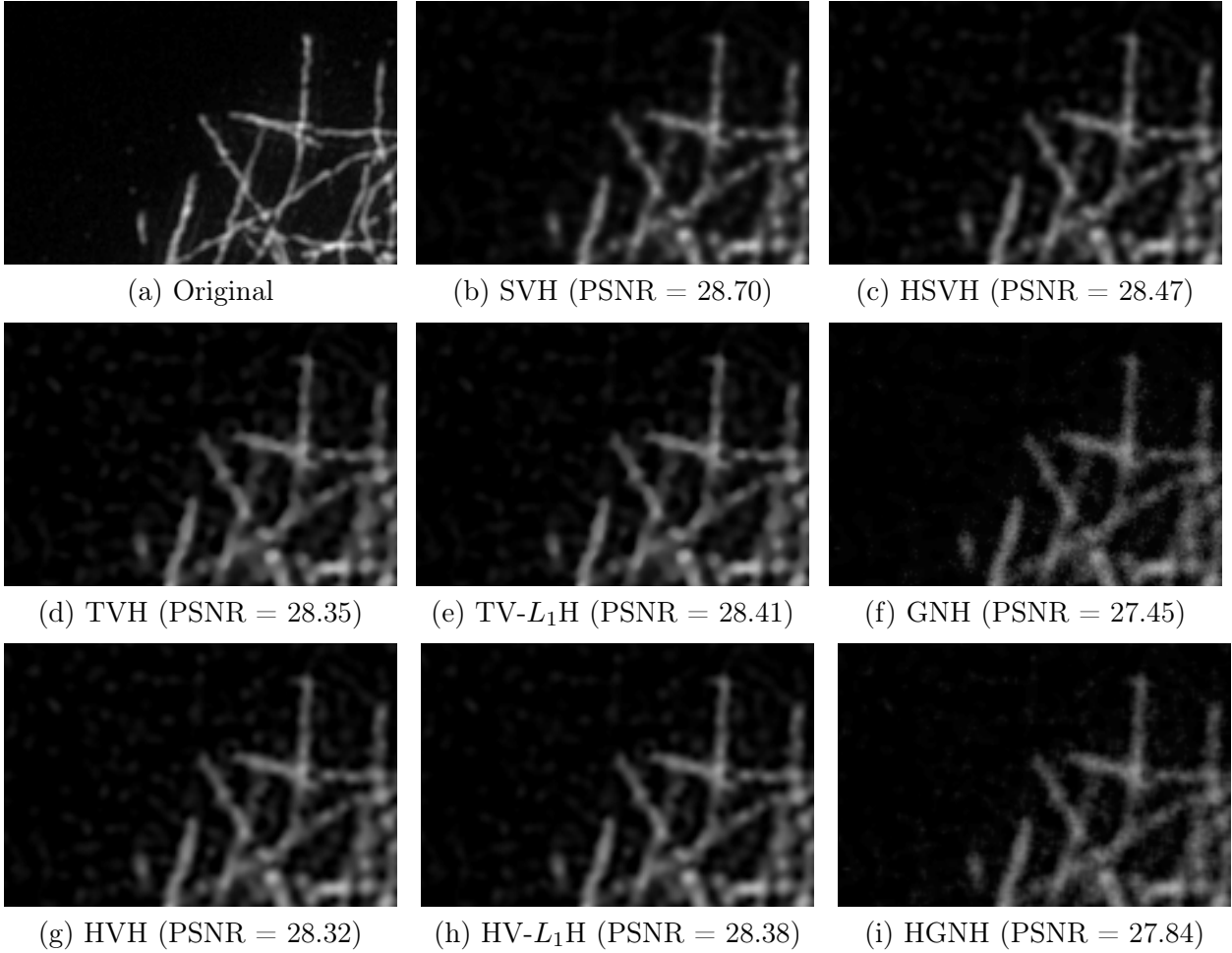


FIGURE 4 – **Deconvolution results on the microtubule image obtained with Huber-based smooth approximation of some convex regularizers.** The original image (available at <http://www.cellimagelibrary.org/> with identifier CIL 36147) is degraded by a Gaussian PSF with standard deviation $\sigma_{\text{PSF}} = 2$ and an additive zero-mean Gaussian noise ($\sigma = 0.04$). Zoom on filament details is shown in order to compare the performance of each method.

magnitude of several deconvolution results shown in Fig. 2. We can clearly notice that, in the case of TV and TV- L_1 solution (see Figs. 3(b) and 3(c) respectively), the gradient vanishes for most of pixels except along object edges, thus implying blocking artifacts. The gradient of HV solution shown in Fig. 3(f) possesses piecewise constant magnitude, or in other words, HV pushes the well-known staircasing effect to the image first-order differentials instead of the image itself. Unlike these regularizers, SV approach, which produces results with smoothly varied gradients as depicted in Fig. 3(e), allows to handle smooth intensity changes and then restore a wider class of images than piecewise constant or piecewise linear images. In comparison, the spatial gradient of GraphNet solution (see Fig. 3(d)) is rather similar to SV, but the magnitude is slightly smaller at some points, resulting in slightly more blurred details.

Regarding second-order regularization, HV- L_1 solution shown in Fig. 2(j) is visually similar to HV, but with less light-shaded spots when compared to TV and TV- L_1 . Hessian-based GraphNet produces quasi-identical results to those obtained with its first-order version (see Figs. 2(k) and

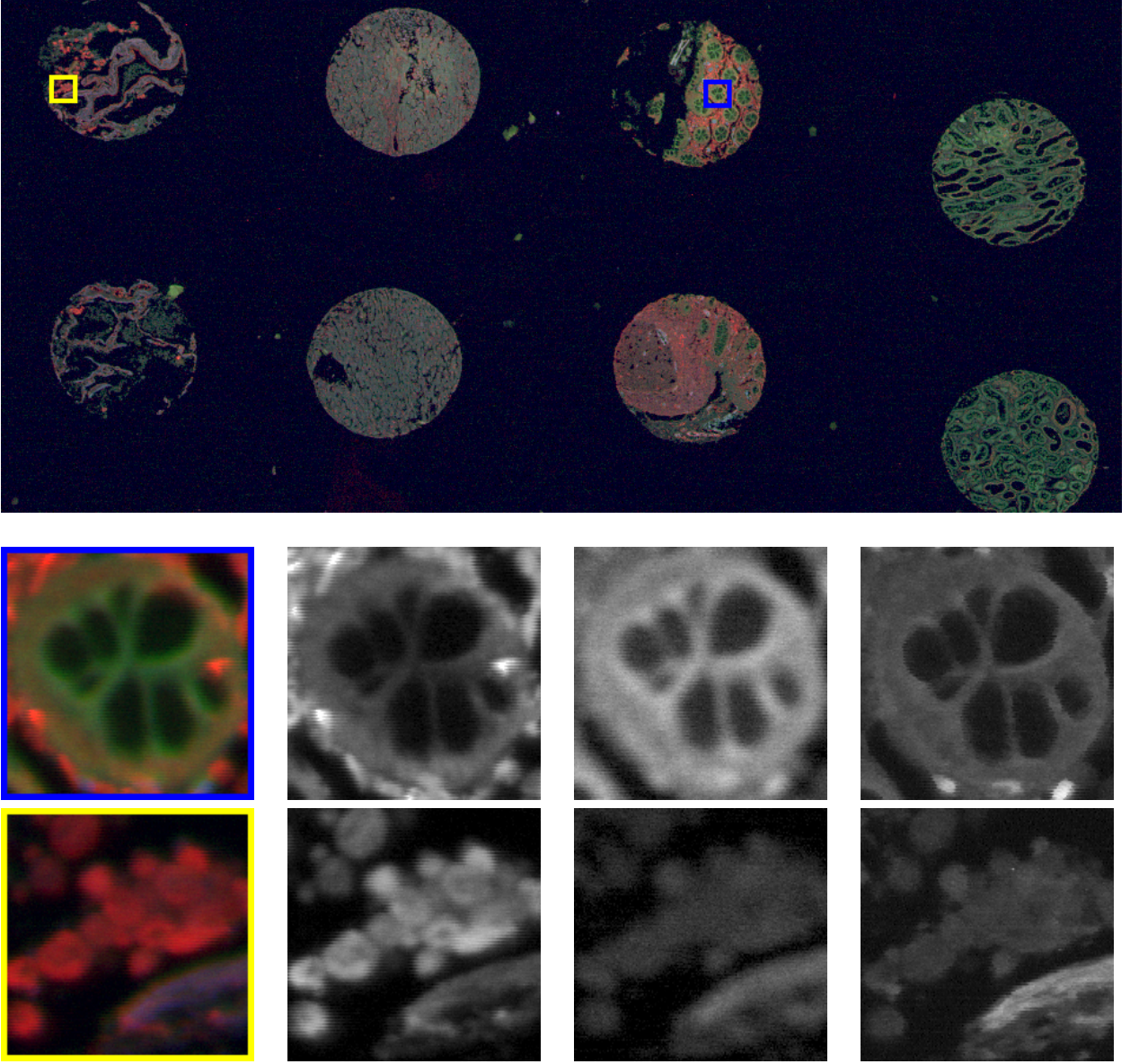


FIGURE 5 – **Three-color fluorescence image of 8 tissue microarray cores.** A region of interest of $4.7 \times 2.8 \text{ mm}^2$ was scanned using the fluorescence scanner named InnoScan 1100AL equipped with three excitation wavelengths (488 nm, 532 nm and 635 nm) at the spatial resolution $0.5 \mu\text{m}/\text{pixel}$, corresponding to an image of 9544×4704 pixels. Two areas which are bordered by blue and yellow box are selected for comparison in details. First row : full size image. Second and third rows : zoom-in views of two selected areas; from left to right : 3 colors at the same time, red (488 nm), green (532 nm) and blue (635 nm) channels displayed separately.

2(h) respectively). This is probably due to the quadratic nature of the squared norms (the L_2 norm for GraphNet and the Frobenius norm for the Hessian-based variant), regardless of the order of considered differentiation operator. In addition, insignificantly different results are also observed in the case of sparse variation and its Hessian-based version (see Figs. 2(l) for SV solution and 2(m) for those obtained with HSV). We note that the difference between them in terms of quantitative evaluation is negligible : only 0.07 dB of difference between the PSNR scores and 0.001 for their SSIM performances.

Finally, we compare the original non-smooth regularizers with the corresponding Huber-norm-based smooth approximation. Figure 4 shows the deconvolution results obtained with these smooth regularization functionals on the microtubule image CIL 36147 degraded by Gaussian PSF ($\sigma_{\text{PSF}} = 2$) and additive Gaussian noise ($\sigma = 0.04$). As depicted in Fig. 4(c), TV-Huber prevents blocking artifact and provides visibly better result than the original TV model, as expected. The main drawback is the light-shaded spot issue that we have previously observed in the case of TV, TV- L_1 and HV solution (see Figs. 2(f), 2(g), and 2(i) respectively). In comparison, the TV- L_1 Huber solution shown in Fig. 4(d), is indistinguishable from those obtained with TV-Huber in terms of fine detail reconstruction as well as non-homogeneous background. We notice that this regularization does not preserve the feature selection property of TV- L_1 , maybe because the Huber norm disables the sparsity induced by the L_1 norm. Concerning second-order approaches, HV-Huber and HV- L_1 Huber give results (see Figs. 4(f) and 4(g) respectively) which are visually similar to their first-order versions. Nevertheless, they tend to worsen the problem of light-shaded spots by making these spots more pronounced. Similarly, undesirable light-shaded spots are also observed in the case of SV-Huber and HSV-Huber solution (see Figs. 4(b) and 4(c)). It degrades sharply the visual quality of these deconvolution results although fine details, such as filament structures are adequately restored. Solutions obtained with GraphNet-Huber and its Hessian-based variant (Figs. 4(e) and 4(h)) do not severely suffer from light-shaded spot issue and have more homogeneous background. However, they can not be considered as reliable solution due to the noisy reconstruction of relevant details in the image foreground. In our opinion, the Huber-norm-based approximation of convex non-smooth regularizers may improve deconvolution results in some aspects as we have observed, but it also modifies the properties of its corresponding original version.

To sum up, the proposed SV-based deconvolution approach yields better results in overall in comparison to those obtained with the tested methods. Not only achieving competitive PSNR and SSIM performance in most of cases, the SV and HV solutions are also very encouraging in terms of visual quality. According to our observations, they avoid in general over-smoothing and over-sharpening effect arising when using other regularizers, while being able to well restore image details with smooth changes of intensities and to efficiently eliminate strong noise from the background.

5.2 Application to real large fluorescence images

We present in this section the deconvolution results obtained with our method on real fluorescence images of tissue microarray (TMA) These TMA images, shown in Fig. 5 and 7, are acquired using dedicated scanner called InnoScan 1100AL². Equipped with three excitation lasers with corresponding wavelength 488 nm (red), 532 nm (green) and 635 nm (blue) respectively, this fluorescence scanner is able to provide single-color as well as multi-color (up to three color) images at very high resolutions. The highest resolution can reach to 0.5 μm per pixel (or a 20X objective equivalently) for normal users and eventually 0.2 μm per pixel in advanced mode for developers.

2. InnoScan 1100AL is developed and commercialized by Innopsys Inc., see <https://www.innopsys.com/en/lifesciences-products/microarrays/innoscan/innoscan-1100-al> for more technical details.

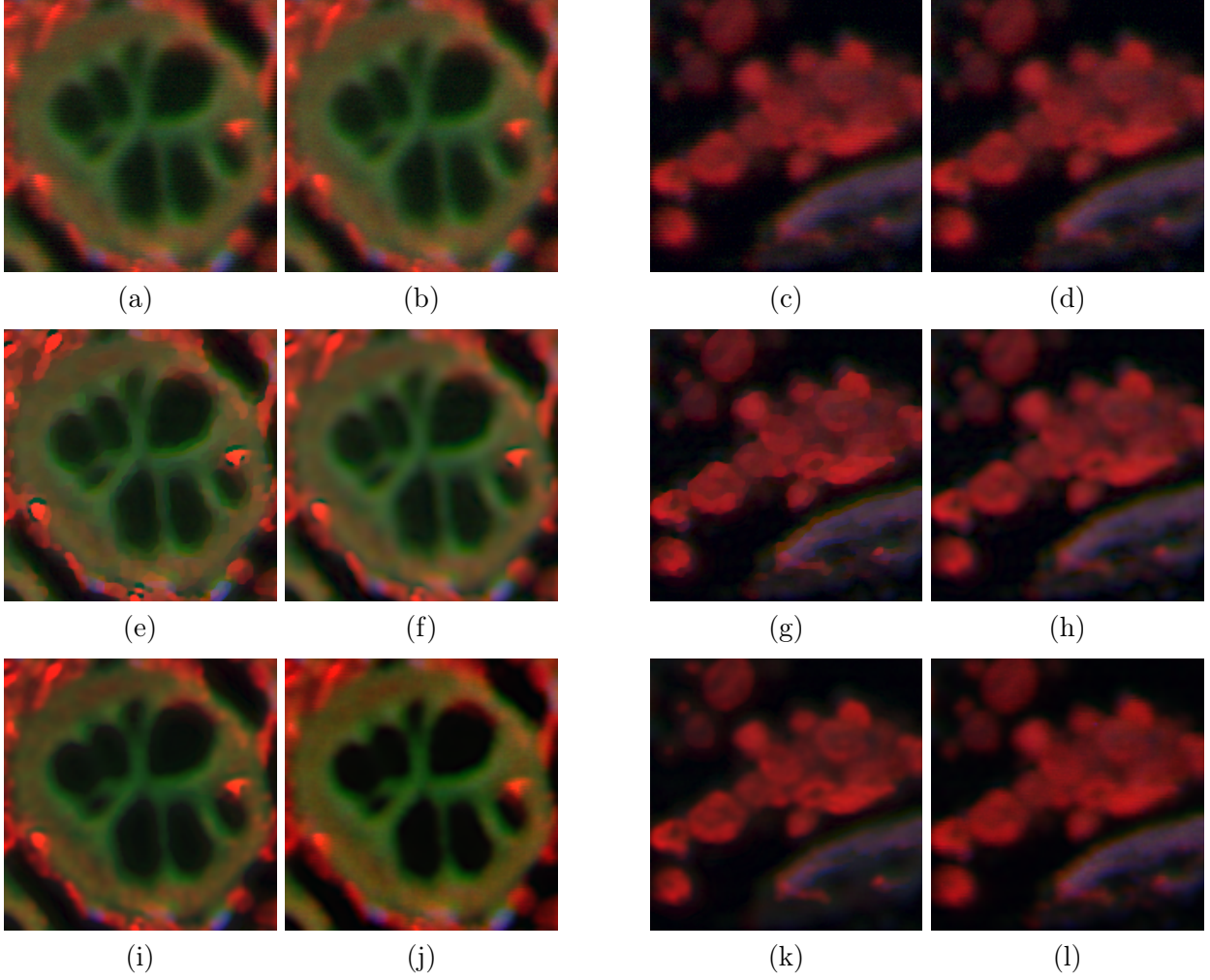


FIGURE 6 – **Deconvolution results on the three-color TMA image obtained with different regularizers.** Zoom-in view on two selected areas are displayed for comparison purposes. (a) and (c) : original acquired image ; (b) and (d) : deconvolution results ; (e) and (g) : TV solution ; (f) and (h) : HV solution ; (i) and (k) : SV solution ; (j) and (l) : LHSV solution.

According to the scanner design, the acquisition on each color channel is performed pixel by pixel, by moving the excitation laser beam with respect to a programmed scanning trajectory and collecting re-emitted light at specific positions on the scanning trajectory. Due to the beam divergence, the intensity of a pixel does not measure the emitted fluorescence signals at its spatial positions but the integral of signals over a wider area defined by the laser pattern which has in theory the shape of an isotropic Gaussian spot. Given that, the diameter of laser spots configured for this fluorescence scanner is typically set to more than $1\ \mu m$, in the case of high-precision scanning which requires sub-micrometer pixel size, the optical resolution (in the sense of the shortest distance between two points that can still be distinguished) is then limited by the laser spot size, resulting in blurred details on acquired images. If the image pixels are correctly positioned, each channel of an acquired image can be modeled as the convolution product of the underlying fluorescently-tagged specimen and the corresponding laser spot. The latter is therefore called the PSF of the associated color channel. Due to its Gaussian nature, this PSF can be parametrized by its FWHM (Full Width at Half Maximum) value which is usually empirically measured during the scanner calibration process. The relation between the FWHM and the standard deviation σ_{PSF} of a Gaussian PSF is given by $\text{FWHM} = 2\sigma_{\text{PSF}}\sqrt{2\log 2}$.

As depicted in the second and third rows of Fig. 5, we notice that the acquired TMA images for this experiment suffer not only from blur, but also from rolling effect (jitter) in vertical direction due to the bad positioning of pixels. A dejittering step is thus required as pre-processing in order to re-align jagged shapes and produce less jittered input images for deconvolution step. To that end, we utilized the algorithm described in [58] to compensate the specific jitter arising on these fluorescence images. In Figs. 6(b) and 6(d), we provide zoom-in views of two selected areas on result obtained with this dejittering algorithm on the three-color TMA image shown in Fig. 5 for illustration purpose. We can clearly see that the rolling effect is significantly reduced when compared to the original jittered images.

Comparison with existing regularizers

We visually compared the results obtained with SV to those obtained with existing state-of-the-art regularizers such as TV, TV- L_1 , GraphNet, HV, and LHSV on a fluorescence image showing eight tissue microarray cores (see Fig. 5). The considered TMA image, saved in 16-bit-TIFF format, was acquired in three colors at the resolution of $0.5\ \mu m$ per pixel with a total size of 9544×4704 pixels. Since we notice that the vertical rolling effect is not the same on the three color channels, as shown in the two bottom rows of Fig. 5, the experiment is performed as the following. Each channel is first dejittered separately for an appropriate removal of the jitter arising on it. Second, the dejittered outcome on each channel served as the input image for deconvolution. The deconvolution results are finally merged to produce a three-color image as the original image for comparison purposes. According to the scanner calibration, the measured FWHM value of the Gaussian laser spot is approximately $0.703\ \mu m$ for all three channels, corresponding to a standard deviation $\sigma_{\text{PSF}} \simeq 0.5971\ \mu m$ which is slightly larger than the image pixel size.

The deconvolution results are shown in Fig. 6 (zoom-in view) on two selected areas for comparison in details. The regularization parameter for each regularization approach is tuned to get the most pleasant visual effect. As shown in Figs. 6(e) and 6(g), TV produces piecewise constant reconstruction which wipes out details in areas with small changes of intensities and over-sharpens the transition between contiguous regions. The restored images look like cartoon images and are not natural visually. HV is able to restore better these fine details with smooth variations while preserving the contrast between structures in the foreground and the background (see Figs. 6(f) and

6(h)). The resulting image seems however slightly blurred when comparing with the SV and LHSV solution. Up to our knowledge, it may be due to the piecewise linear nature of the HV solution which does not fit the smooth nature of structures on the underlying image.

Both LHSV and SV which penalize jointly image intensities and image differential components, provide sharper reconstruction than HV based on the second-order differentiation operator. Because of this joint penalization concept, they also tend to unfortunately over-sparsify the distribution of non-zero pixels, resulting in vanishing nearly-zero-intensity details, as noticeable in Fig. 6(i) and 6(j) where several green color features are nearly disappeared. We remark that the over-sparsifying effect on LHSV solution is slightly stronger than those obtained with SV. In our opinion, it is mainly due to the combination of the logarithm function and the squared L_2 norm in the LHSV functional in comparison to the L_2 norm in the case of SV. Note that the jittering was not completely removed on the example shown in Figs. 6(b) and 6(d), but SV handles these imperfect input images and produces nearly jitter-free solutions (see Figs. 6(i), and 6(k)). It was not possible to get such a result with LHSV (see Figs. 6(j), and 6(l)).

Sensitivity to PSF parameters

As previously reported, when the PSF of the imaging system is known, SV approach appears to be the best solution for deconvolution of real fluorescence images. There is unfortunately a small chance that the PSF is known with a very high precision. In practice, the PSF is rather estimated by direct estimation on acquired images or by calibration using small point-like objects to get PSF measures at different location. In fluorescence microscopy, one usually considers microbeads to estimate the PSF of the underlying microscope. However, this estimation may in some cases suffer from severe errors due to the measurement conditions and can lead to poor deconvolution results if the used deconvolution method is too sensitive to errors in the estimation of the PSF.

Consequently, our interest here is to evaluate the sensitivity of SV deconvolution to the PSF parameters. To that end, we consider a TMA image, shown in Fig. 7, which was acquired on the green channel (532 nm) at the resolution of 0.2 μm per pixel using InnoScan 1100AL scanner. In this experiment, we note that the PSF of the scanner was not measured before acquisition. In Fig. 8, we provide then comparative results obtained on this single-color image with different PSFs to better appreciate the impact of PSF change on the deconvolution results. In this particular study, it has been experimentally established that the PSF can be approximated by an isotropic Gaussian function. Hence, we generated several Gaussian PSFs by varying the FWHM value in the range of $\{0.6, 0.7, 0.8, 0.9, 1.0\}$ (in μm). Regarding the regularization parameter λ , we selected four typical values to control the regularization level : $\lambda \in \{0.002, 0.003, 0.005, 0.008\}$.

In Fig. 8, we remark first that, for all the considered FWHM values and regularization parameters, our algorithm produced encouraging deconvolution results in terms of visual quality. However, we realize that some results still suffer from vertical rolling effect because jitter is not completely removed after pre-processing, as shown in the first row of Fig. 8. This effect is typically observed on deconvolved images obtained with low FWHM values. In the special case where $FWHM = 0.6$, all the four deconvolved images are concerned (see the second row of Fig. 8). The jittering artifacts are less visible with larger FWHM or when increasing the regularization parameters. The setting $FWHM = 1.0$ and $\lambda = 0.008$ yields the best visual results in comparison to those obtained with the other combinations of parameters. Although, very similar results are obtained for $FWHM > 0.08$, irrespectively to the choice of λ . This experiments revealed that the SV-based deconvolution method is not sensitive to small errors in PSF estimation and to non-stationarities induced by mixed Poisson-Gaussian noise.

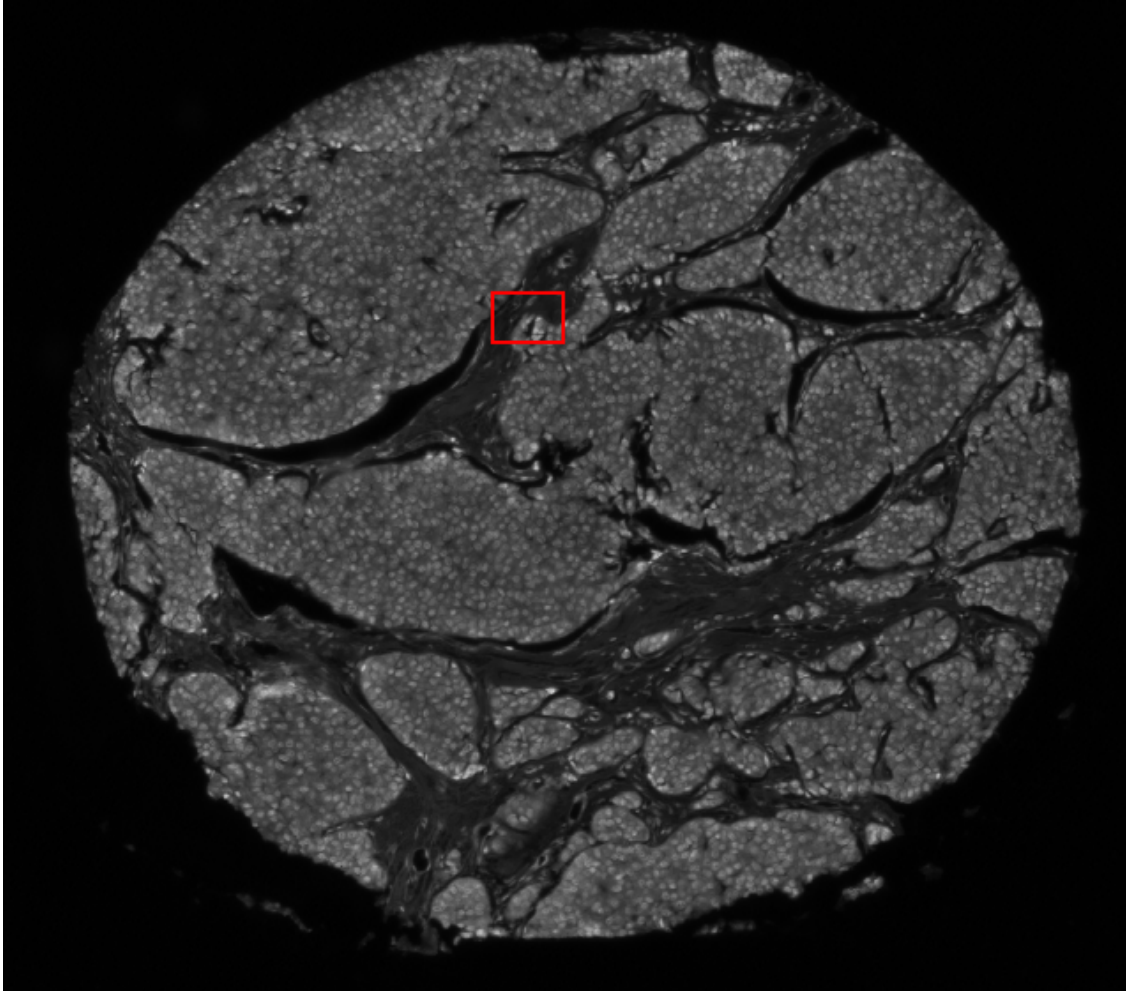


FIGURE 7 – **Single-color fluorescence TMA image.** Image of a TMA core is acquired on the green channel (532 nm) at the resolution 0.2 μm per pixel. The size of the acquired image is 7580×6870 pixels. A region (bordered by red box) is selected for comparison in details of deconvolution results obtained with different PSFs.

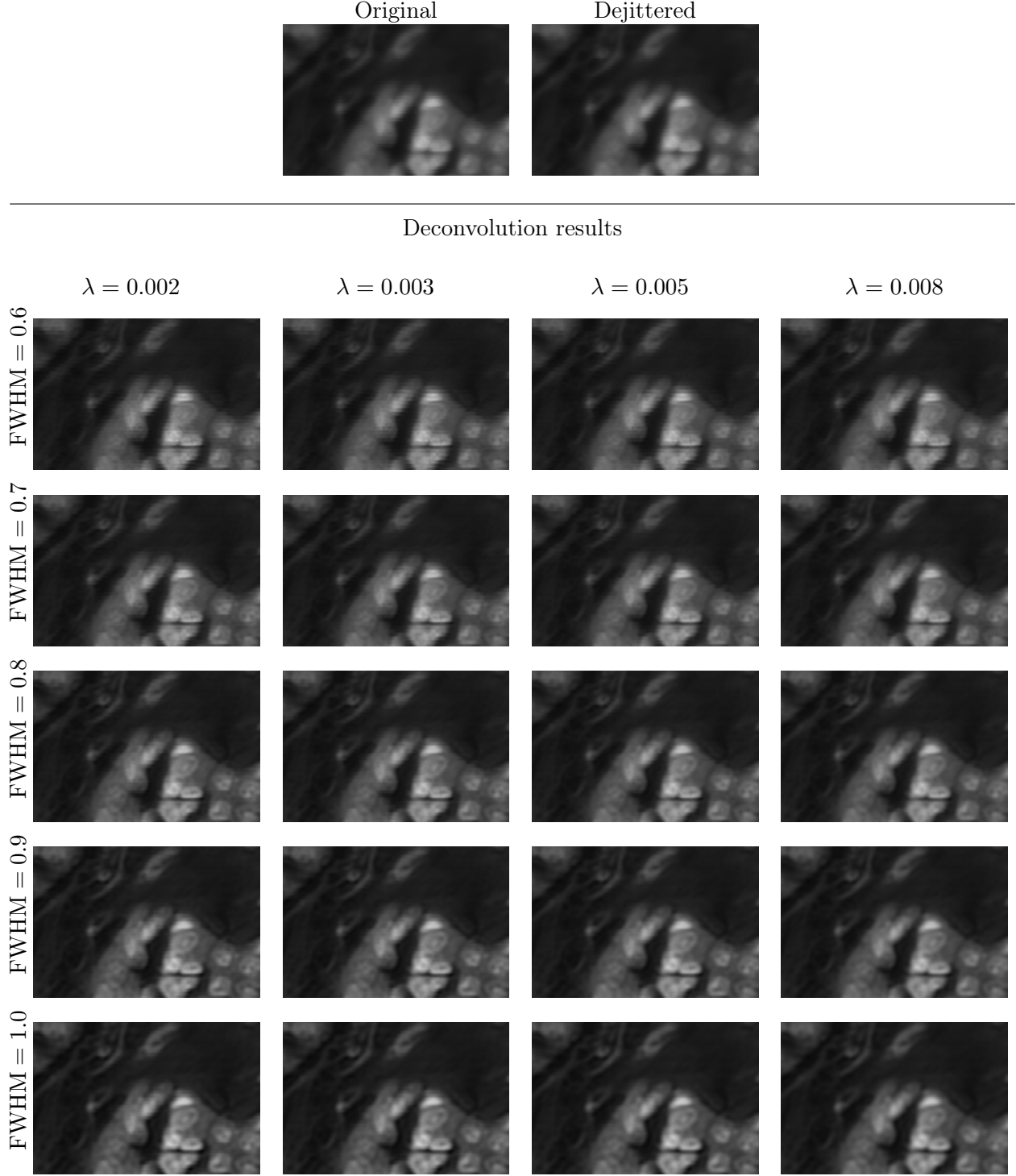


FIGURE 8 – **Comparison of deconvolution results obtained on the single-color TMA image with different PSFs and regularization parameters.** Zoom-in view on the selected area (bordered by red box in Fig. 7) to compare in details before/after deconvolution differences as well as results obtained with different parameters. We consider Gaussian PSFs with FWHM values varying in the range $\{0.6, 0.7, 0.8, 0.9, 1.0\}$ and several regularization parameters $\lambda \in \{0.002, 0.003, 0.005, 0.008\}$. The two values, FWHM = 1.0 and $\lambda = 0.008$, yield the best result in terms of visual quality compared to the other combinations of parameters.

In terms of computational performance, the proposed SV-based deconvolution algorithm takes only 0.5-0.7 second, for both first-order and second-order variants, on a standard image of 512×512 pixels. This processing time is comparable to TV with about 0.6 second and is much more faster than HV with more than 1.3 seconds. Regarding LHSV approach, the computational time can reach more than 2.4 seconds, due to the non-convex nature of the regularization functional. The method was applied to large fluorescence images (7590×6870 pixels) and the computation time was about 80 seconds with an unoptimized implementation (no patch decomposition, no threading implementation) of our method in Matlab. The experiments were performed on a Macbook Pro equipped with 2.7 Ghz Intel Core i7, 16 Gb of RAM and the Mac OS X v.10.12.4 operating system. All the tested algorithms were implemented in Matlab and we exploited the intrinsic parallelism of the CPU to deal with large-scale inverse problems.

6 Conclusion

In this paper, we have presented a deconvolution method for 2D fluorescence imaging using a novel family of convex regularizers. The proposed regularization functionals are based from the concept of sparse variation, that consists in penalizing jointly the image intensity and gradient at each pixel to favor the co-localization of non-zero intensities and gradients, by considering eventually higher-order differentiation operators. By construction, these regularizers possess interesting mathematical properties, namely convexity, invariance to scale, rotation, and translation as the well-known total variation regularization approach. It allows therefore to design efficient algorithms to solve the underlying deconvolution problem which is in general large-scale in the context of fluorescence microscopy. We reformulated the deconvolution as a minimization problem of a convex energy function composed of a quadratic data fidelity term and a sparse-variation-based regularity term under the constrain of positivity and maximum intensity value. In order to minimize this energy, we considered a primal-dual (proximal) algorithm based on the full-splitting technique which only involves first-order operators to cope with the large-scale nature of the problem. Experimental results on both synthetic and real fluorescence images demonstrated that our proposed method was able to produce very competitive deconvolution results when compared to several competing methods in terms of quantitative performance as well as visual quality and computational time.

7 Adjoint operators of discrete directional derivatives

Let $L : \mathcal{X} \rightarrow \mathcal{X}$ be a linear operator defined on the vector space $\mathcal{X} = \mathbb{R}^{MN}$, its adjoint operator L^\top satisfies the equation $\langle Lu, w \rangle_{\mathcal{X}} = \langle u, L^\top w \rangle_{\mathcal{X}}, \forall (u, w) \in \mathcal{X} \times \mathcal{X}$. If we consider the discrete directional derivatives defined in (25a)-(25e), their corresponding adjoint is therefore given by :

$$[(D_1^{(1)})^\top w]_{i,j} = \begin{cases} w_{i,j} & \text{if } i = 1 \\ w_{i,j} - w_{i-1,j} & \text{if } 1 < i < M \\ -w_{i-1,j} & \text{if } i = M \end{cases}$$

$$[(D_2^{(1)})^\top w]_{i,j} = \begin{cases} w_{i,j} & \text{if } j = 1 \\ w_{i,j} - w_{i,j-1} & \text{if } 1 < j \leq N \\ -w_{i,j-1} & \text{if } j = N \end{cases}$$

and

$$[(D_{1,1}^{(2)})^\top w]_{i,j} = \begin{cases} w_{i+1,j} - 2w_{i,j} - w_{i-1,j} & \text{if } 1 < i < M \\ 0 & \text{otherwise} \end{cases}$$

$$[(D_{2,2}^{(2)})^\top w]_{i,j} = \begin{cases} w_{i,j+1} - 2w_{i,j} - w_{i,j-1} & \text{if } 1 < j < N \\ 0 & \text{otherwise} \end{cases}$$

$$[(D_{1,2}^{(2)})^\top w]_{i,j} = [(D_{2,1}^{(2)})^\top w]_{i,j}$$

$$= \begin{cases} w_{i,j} & \text{if } i = 1, j = 1; \\ w_{i,j} - w_{i,j-1} & \text{if } i = 1, \\ & 1 < j < N; \\ -w_{i,j-1} & \text{if } i = 1, j = N; \\ w_{i,j} - w_{i-1,j} & \text{if } 1 < i < M, \\ & j = 1; \\ w_{i,j} - w_{i-1,j} - w_{i,j-1} + w_{i-1,j-1} & \text{if } 1 < i < M, \\ & 1 < j < N; \\ -w_{i,j-1} + w_{i-1,j-1} & \text{if } 1 < i < M, \\ & j = N; \\ -w_{i-1,j} & \text{if } i = M, j = 1; \\ -w_{i-1,j} + w_{i-1,j-1} & \text{if } i = M, \\ & 1 < j < N; \\ w_{i-1,j-1} & \text{if } i = M, j = N. \end{cases}$$

Références

- [1] M. Eickenberg, E. Dohmatob, B. Thirion, and G. Varoquaux, “Grouping total variation and sparsity : Statistical learning with segmenting penalties,” in *Medical Image Computing and Computer-Assisted Intervention – MICCAI 2015 : 18th International Conference, Munich, Germany, October 5-9, 2015, Proceedings, Part I*, N. Navab, J. Hornegger, W. M. Wells, and A. Frangi, Eds. Cham : Springer International Publishing, 2015, pp. 685–693. [Online]. Available : http://dx.doi.org/10.1007/978-3-319-24553-9_84
- [2] L. I. Rudin, S. Osher, and E. Fatemi, “Nonlinear total variation based noise removal algorithms,” *Physica D : Nonlinear Phenomena*, vol. 60, no. 1, pp. 259 – 268, 1992. [Online]. Available : <http://www.sciencedirect.com/science/article/pii/016727899290242F>
- [3] S. Lefkimmatis, J. P. Ward, and M. Unser, “Hessian Schatten-norm regularization for linear inverse problems,” *IEEE Transactions on Image Processing*, vol. 22, no. 5, pp. 1873–1888, May 2013.
- [4] H. T. M. van der Voort and K. C. Strasters, “Restoration of confocal images for quantitative image analysis,” *Journal of Microscopy*, vol. 178, no. 2, pp. 165–181, 1995. [Online]. Available : <http://dx.doi.org/10.1111/j.1365-2818.1995.tb03593.x>
- [5] G. M. P. van Kempen, H. T. M. van der Voort, J. G. J. Bauman, and K. C. Strasters, “Comparing maximum likelihood estimation and constrained Tikhonov-Miller restoration,” *IEEE Engineering in Medicine and Biology Magazine*, vol. 15, no. 1, pp. 76–83, Jan 1996.

- [6] G. M. P. van Kempen, L. J. van Vliet, P. J. Verveer, and H. T. M. van der Voort, "A quantitative comparison of image restoration methods for confocal microscopy," *Journal of Microscopy*, vol. 185, no. 3, pp. 354–365, 1997. [Online]. Available : <http://dx.doi.org/10.1046/j.1365-2818.1997.d01-629.x>
- [7] W. A. Carrington, "Image restoration in 3-D microscopy with limited data," in *Proc. SPIE*, vol. 1205, 1990. [Online]. Available : <http://dx.doi.org/10.1117/12.17785>
- [8] W. A. Carrington, R. M. Lynch, E. D. Moore, G. Isenberg, K. E. Fogarty, and F. S. Fay, "Superresolution three-dimensional images of fluorescence in cells with minimal light exposure," *Science*, vol. 268, no. 5216, pp. 1483–1487, 1995. [Online]. Available : <http://science.sciencemag.org/content/268/5216/1483>
- [9] E. S. Meinel, "Origins of linear and nonlinear recursive restoration algorithms," *Journal of the Optical Society of America A*, vol. 3, no. 6, pp. 787–799, Jun 1986. [Online]. Available : <http://josaa.osa.org/abstract.cfm?URI=josaa-3-6-787>
- [10] W. H. Richardson, "Bayesian-based iterative method of image restoration," *Journal of the Optical Society of America*, vol. 62, no. 1, pp. 55–59, Jan 1972. [Online]. Available : <http://www.osapublishing.org/abstract.cfm?URI=josa-62-1-55>
- [11] L. B. Lucy, "An iterative technique for the rectification of observed distributions," *The Astrophysical Journal*, vol. 79, no. 6, pp. 745–754, Jun. 1974.
- [12] L. A. Shepp and Y. Vardi, "Maximum likelihood reconstruction for emission tomography," *IEEE Transactions on Medical Imaging*, vol. 1, no. 2, pp. 113–122, Oct 1982.
- [13] J.-B. Sibarita, *Deconvolution Microscopy*. Berlin, Heidelberg : Springer Berlin Heidelberg, 2005, pp. 201–243. [Online]. Available : <https://doi.org/10.1007/b102215>
- [14] P. L. Combettes and J. C. Pesquet, "Image restoration subject to a total variation constraint," *IEEE Transactions on Image Processing*, vol. 13, no. 9, pp. 1213–1222, 2004.
- [15] N. Dey, L. Blanc-Feraud, C. Zimmer, P. Roux, Z. Kam, J. Olivo-Marin, and J. Zerubia, "Richardson-lucy algorithm with total variation regularization for 3d confocal microscope deconvolution," *Microscopy Research Technique*, vol. 69, no. 4, pp. 260–266, 2006.
- [16] F. Soulez, L. Denis, Y. Tourneur, and É. Thiébaud, "Blind deconvolution of 3D data in wide field fluorescence microscopy," in *International Symposium on Biomedical Imaging*, Barcelone, Spain, May 2012.
- [17] T. Chan, A. Marquina, and P. Mulet, "High-order total variation-based image restoration," *SIAM Journal on Scientific Computing*, vol. 22, no. 2, pp. 503–516, 2000.
- [18] S. Lefkimiatis, A. Bourquard, and M. Unser, "Hessian-based norm regularization for image restoration with biomedical applications," *IEEE Transactions on Image Processing*, vol. 21, no. 3, pp. 983–995, March 2012.
- [19] S. Lefkimiatis and M. Unser, "Poisson image reconstruction with Hessian Schatten-norm regularization," *IEEE Transactions on Image Processing*, vol. 22, no. 11, pp. 4314–4327, Nov 2013.
- [20] M. Arigovindan, J. C. Fung, D. Elnatan, V. Mennella, Y.-H. M. Chan, M. Pollard, E. Brånlund, J. W. Sedat, and D. A. Agard, "High-resolution restoration of 3D structures from widefield images with extreme low signal-to-noise-ratio," *Proceedings of the National Academy of Sciences*, vol. 110, no. 43, pp. 17344–17349, 2013. [Online]. Available : <http://www.pnas.org/content/110/43/17344.abstract>

- [21] S. F. Gull and G. J. Daniell, "Image reconstruction from incomplete and noisy data," *Nature*, vol. 272, no. 5655, pp. 686–690, 04 1978. [Online]. Available : <http://dx.doi.org/10.1038/272686a0>
- [22] J.-L. Starck and F. Murtagh, *Astronomical Image and Data Analysis*. Berlin, Heidelberg : Springer Berlin Heidelberg, 2006. [Online]. Available : https://doi.org/10.1007/978-3-540-33025-7_3
- [23] N. Zhao, Q. Wei, A. Basarab, D. Kouamé, and J. Y. Tournieret, "Single image super-resolution of medical ultrasound images using a fast algorithm," in *2016 IEEE 13th International Symposium on Biomedical Imaging (ISBI)*, April 2016, pp. 473–476.
- [24] A. C. Kokaram, N. Persad, J. Lasenby, W. J. Fitzgerald, A. McKinnon, and M. Welland, "Restoration of images from the scanning-tunneling microscope," *Applied Optics*, vol. 34, no. 23, pp. 5121–5132, Aug 1995. [Online]. Available : <http://ao.osa.org/abstract.cfm?URI=ao-34-23-5121>
- [25] M. Vauhkonen, D. Vadasz, P. A. Karjalainen, E. Somersalo, and J. P. Kaipio, "Tikhonov regularization and prior information in electrical impedance tomography," *IEEE Transactions on Medical Imaging*, vol. 17, no. 2, pp. 285–293, April 1998.
- [26] L. Ying, D. Xu, and Z. P. Liang, "On Tikhonov regularization for image reconstruction in parallel MRI," in *The 26th Annual International Conference of the IEEE Engineering in Medicine and Biology Society*, vol. 1, Sept 2004, pp. 1056–1059.
- [27] G. A. G. Cidade, C. Anteneodo, N. C. Roberty, and A. J. S. Neto, "A generalized approach for atomic force microscopy image restoration with Bregman distances as Tikhonov regularization terms," *Inverse Problems in Engineering*, vol. 8, no. 5, pp. 457–472, 2000. [Online]. Available : <http://dx.doi.org/10.1080/174159700088027741>
- [28] S. Boyd and L. Vandenberghe, *Convex Optimization*. New York, NY, USA : Cambridge University Press, 2004.
- [29] M. Nikolova, "Weakly constrained minimization : Application to the estimation of images and signals involving constant regions," *Journal of Mathematical Imaging and Vision*, vol. 21, no. 2, pp. 155–175, Sep 2004. [Online]. Available : <https://doi.org/10.1023/B:JMIV.0000035180.40477.bd>
- [30] C. Louchet and L. Moisan, "Posterior expectation of the total variation model : Properties and experiments," *SIAM Journal on Imaging Sciences*, vol. 6, no. 4, pp. 2640–2684, 2013. [Online]. Available : <https://doi.org/10.1137/120902276>
- [31] R. Bhatia, *A Review of Linear Algebra*. New York, NY : Springer New York, 1997, pp. 1–27. [Online]. Available : https://doi.org/10.1007/978-1-4612-0653-8_1
- [32] S. Delpretti, F. Luisier, s. Ramani, T. Blu, and M. Unser, "Multiframe sure-let denoising of timelapse fluorescence microscopy images," in *2008 IEEE 13th International Symposium on Biomedical Imaging (ISBI)*, Paris, France, May 2008, pp. 149–152.
- [33] J. Boulanger, C. Kervrann, P. Bouthemy, P. Elbau, J. B. Sibarita, and J. Salamero, "Patch-based nonlocal functional for denoising fluorescence microscopy image sequences," *IEEE Transactions on Medical Imaging*, vol. 29, no. 2, pp. 442–454, Feb 2010.
- [34] M. Makitalo and A. Foi, "Optimal inversion of the generalized anscombe transformation for poisson-gaussian noise," *IEEE Transactions on Image Processing*, vol. 22, no. 1, pp. 91–103, 2013.

- [35] F. Dupe, J. Fadili, and J. Starck, “A proximal iteration for deconvolving poisson noisy images using sparse representations,” *IEEE Transactions on Image Processing*, vol. 18, no. 2, pp. 310–321, 2009.
- [36] A. Chambolle and T. Pock, “A first-order primal-dual algorithm for convex problems with applications to imaging,” *Journal of Mathematical Imaging and Vision*, vol. 40, no. 1, pp. 120–145, 2011. [Online]. Available : <http://dx.doi.org/10.1007/s10851-010-0251-1>
- [37] L. Condat, “A primal–dual splitting method for convex optimization involving lipschitzian, proximable and linear composite terms,” *Journal of Optimization Theory and Applications*, vol. 158, no. 2, pp. 460–479, Aug 2013. [Online]. Available : <http://dx.doi.org/10.1007/s10957-012-0245-9>
- [38] M. Heideman, D. Johnson, and C. Burrus, “Gauss and the history of the fast Fourier transform,” *IEEE ASSP Magazine*, vol. 1, no. 4, pp. 14–21, October 1984.
- [39] C. Van Loan, *Computational Frameworks for the Fast Fourier Transform*. Society for Industrial and Applied Mathematics, 1992. [Online]. Available : <http://epubs.siam.org/doi/abs/10.1137/1.9781611970999>
- [40] M. Frigo and S. G. Johnson, “FFTW : an adaptive software architecture for the FFT,” in *Proceedings of the 1998 IEEE International Conference on Acoustics, Speech and Signal Processing*, vol. 3, May 1998, pp. 1381–1384.
- [41] —, “The design and implementation of FFTW3,” *Proceedings of the IEEE*, vol. 93, no. 2, pp. 216–231, Feb 2005.
- [42] P. L. Combettes, Đ. Dũng, and B. C. Vũ, “Proximity for sums of composite functions,” *Journal of Mathematical Analysis and Applications*, vol. 380, no. 2, pp. 680 – 688, 2011. [Online]. Available : <http://www.sciencedirect.com/science/article/pii/S0022247X11002137>
- [43] P. L. Combettes, L. Condat, J. C. Pesquet, and B. C. Vũ, “A forward-backward view of some primal-dual optimization methods in image recovery,” in *2014 IEEE International Conference on Image Processing (ICIP)*, Oct 2014, pp. 4141–4145.
- [44] B. Mercier, *Lectures on Topics in Finite Element Solution of Elliptic Problems*. Springer-Verlag Berlin Heidelberg, 1979.
- [45] J. Eckstein and D. P. Bertsekas, “On the Douglas–Rachford splitting method and the proximal point algorithm for maximal monotone operators,” *Mathematical Programming*, vol. 55, no. 1, pp. 293–318, 1992. [Online]. Available : <http://dx.doi.org/10.1007/BF01581204>
- [46] P. L. Combettes, “Solving monotone inclusions via compositions of nonexpansive averaged operators,” *Optimization*, vol. 53, pp. 475–504, 2004.
- [47] P. L. Combettes and V. R. Wajs, “Signal recovery by proximal forward-backward splitting,” *SIAM Multiscale Modeling and Simulation*, vol. 4, no. 4, pp. 1168–1200, 2005. [Online]. Available : <https://doi.org/10.1137/050626090>
- [48] P. L. Combettes and J.-C. Pesquet, *Proximal Splitting Methods in Signal Processing*. New York, NY : Springer New York, 2011, pp. 185–212. [Online]. Available : http://dx.doi.org/10.1007/978-1-4419-9569-8_10
- [49] L. Condat, “A generic proximal algorithm for convex optimization – application to total variation minimization,” *IEEE Signal Processing Letters*, vol. 21, no. 8, pp. 985–989, Aug 2014.
- [50] J. J. Moreau, “Proximité et dualité dans un espace hilbertien,” *Bulletin de la Société Mathématique de France*, vol. 93, pp. 273–299, 1965. [Online]. Available : http://www.numdam.org/item?id=BSMF_1965__93__273_0

- [51] H. L. Fu, J. L. Mueller, M. J. Whitley, D. M. Cardona, R. M. Willett, D. G. Kirsch, J. Q. Brown, and N. Ramanujam, "Structured illumination microscopy and a quantitative image analysis for the detection of positive margins in a pre-clinical genetically engineered mouse model of sarcoma," *PLOS ONE*, vol. 11, no. 1, pp. 1–19, 01 2016. [Online]. Available : <https://doi.org/10.1371/journal.pone.0147006>
- [52] D. Sage, L. Donati, F. Soulez, D. Fortun, G. Schmit, A. Seitz, R. Guiet, C. Vonesch, and M. Unser, "DeconvolutionLab2 : an open-source software for deconvolution microscopy," *Methods*, vol. 115, pp. 28–41, 2017.
- [53] B. Ng, A. Vahdat, G. Hamarneh, and R. Abugharbieh, "Generalized sparse classifiers for decoding cognitive states in fMRI," in *Proceedings of the First International Workshop on Machine Learning in Medical Imaging : (MLMI 2010), Held in Conjunction with MICCAI 2010, Beijing, China.,* F. Wang, P. Yan, K. Suzuki, and D. Shen, Eds. Berlin, Heidelberg : Springer Berlin Heidelberg, 2010, pp. 108–115. [Online]. Available : https://doi.org/10.1007/978-3-642-15948-0_14
- [54] B. M. Kandel, D. A. Wolk, J. C. Gee, and B. Avants, "Predicting cognitive data from medical images using sparse linear regression," in *Proceedings of the 23rd International Conference on Information Processing in Medical Imaging (IPMI 2013), Asilomar, CA, USA.,* J. C. Gee, S. Joshi, K. M. Pohl, W. M. Wells, and L. Zöllei, Eds. Berlin, Heidelberg : Springer Berlin Heidelberg, 2013, pp. 86–97. [Online]. Available : https://doi.org/10.1007/978-3-642-38868-2_8
- [55] L. Grosenick, B. Klingenberg, K. Katovich, B. Knutson, and J. E. Taylor, "Interpretable whole-brain prediction analysis with GraphNet," *NeuroImage*, vol. 72, pp. 304–321, 2013. [Online]. Available : <http://www.sciencedirect.com/science/article/pii/S1053811912012487>
- [56] T. F. Chan and S. Esedoglu, "Aspects of total variation regularized L1 function approximation," *SIAM Journal on Applied Mathematics*, vol. 65, no. 5, pp. 1817–1837, 2005. [Online]. Available : <https://doi.org/10.1137/040604297>
- [57] V. Michel, A. Gramfort, G. Varoquaux, E. Eger, and B. Thirion, "Total variation regularization for fMRI-based prediction of behavior," *IEEE Transactions on Medical Imaging*, vol. 30, no. 7, pp. 1328–1340, July 2011.
- [58] H.-N. Nguyen, V. Paveau, C. Cauchois, and C. Kervrann, "A variational method for deblurring large fluorescence line scanner images ," Aug. 2017, working paper or preprint. [Online]. Available : <https://hal.inria.fr/hal-01577139>